Naval Research Laboratory
Washington, DC 20375-5320

NRL/MR/6790--03-8693

Ultrashort Laser Pulses and Electromagnetic Pulse Generation in Air and on Dielectric Surfaces

PHILLIP SPRANGLE
JOSEPH PEÑANO

Beam Physics Branch
Plasma Physics Division

BAHMAN HAFIZI

Icarus Research, Inc.
Bethesda, MD

CHRIS KAPETANAKOS

LET Corp.
Washington, DC

July 28, 2003

20030826 034

Approved for public release; distribution is unlimited.

REPORT DOCUMENTATION PAGE

Form Approved
OMB No. 0704-0188

Public reporting burden for this collection of information is estimated to average 1 hour per response, including the time for reviewing instructions, searching existing data sources, gathering and maintaining the data needed, and completing and reviewing this collection of information. Send comments regarding this burden estimate or any other aspect of this collection of information, including suggestions for reducing this burden to Department of Defense, Washington Headquarters Services, Directorate for Information Operations and Reports (0704-0188), 1215 Jefferson Davis Highway, Suite 1204, Arlington, VA 22202-4302. Respondents should be aware that notwithstanding any other provision of law, no person shall be subject to any penalty for failing to comply with a collection of information if it does not display a currently valid OMB control number. **PLEASE DO NOT RETURN YOUR FORM TO THE ABOVE ADDRESS.**

1. REPORT DATE *(DD-MM-YYYY)*	2. REPORT TYPE	3. DATES COVERED *(From - To)*
July 28, 2003	Interim Report	

4. TITLE AND SUBTITLE

Ultrashort Laser Pulses and Electromagnetic Pulse Generation in Air and on Dielectric Surfaces

5a. CONTRACT NUMBER

5b. GRANT NUMBER

5c. PROGRAM ELEMENT NUMBER

6. AUTHOR(S)

Phillip Sprangle, Joseph Peñano, Bahman Hafizi,* and Chris Kapetanakos†

5d. PROJECT NUMBER

5e. TASK NUMBER

5f. WORK UNIT NUMBER

7. PERFORMING ORGANIZATION NAME(S) AND ADDRESS(ES)

Naval Research Laboratory, Code 6790
4555 Overlook Avenue, SW
Washington, DC 20375-5320

8. PERFORMING ORGANIZATION REPORT NUMBER

NRL/MR/6790--03-8693

9. SPONSORING / MONITORING AGENCY NAME(S) AND ADDRESS(ES)

Office of Naval Research
800 North Quincy Street
Arlington, VA 22217

10. SPONSOR / MONITOR'S ACRONYM(S)

11. SPONSOR / MONITOR'S REPORT NUMBER(S)

12. DISTRIBUTION / AVAILABILITY STATEMENT

Approved for public release; distribution is unlimited.

13. SUPPLEMENTARY NOTES

*Icarus Research, Inc., P.O. Box 30780, Bethesda, MD 20824-0780
†LET Corp., 4431 MacArthur Boulevard, Washington, DC 20007

14. ABSTRACT

Intense, ultrashort laser pulses propagating in the atmosphere have been observed to emit sub-THz elecromagnetic pulses (EMP). The purpose of this paper is to analyze EMP generation from the interaction of ultrashort laser pulses with air and with dielectric surfaces and to determine the efficiency of conversion of laser energy to EMP energy. In our self-consistent model the laser pulse partially ionizes the medium, forms a plasma filament, and through the ponderomotive forces associated with the laser pulse, drives plasma currents which are the source of the EMP. The propagating laser pulse evolves under the influence of diffraction, Kerr focusing, plasma defocusing, and energy depletion due to electron collisions and ionization. Collective effects and recombination processes are also included in the model. The duration of the EMP in air, at a fixed point, is found to be a few hundred femtoseconds, i.e., on the order of the laser pulse duration plus the electron collision time. For steady state laser pulse propagation the flux of EMP energy is non-radiative and axially directed. Radiation EMP energy is present only for non-steady state or transient laser pulse propagation. The analysis also considers the generation of EMP on the surface of a dielectric on which an ultrashort laser pulse is incident. For typical laser parameters, the power and energy conversion efficiency from laser radiation to EMP radiation in both air and from dielectric surfaces is found to be extremely small, $< 10^{-8}$. Results of full scale, self-consistent, numerical simulations of atmospheric and dielectric surface EMP generation are presented. A recent experiment on atmospheric EMP generation is also simulated.

15. SUBJECT TERMS

Electromagnetic pulses; Ultrashort laser pulses; Ionization; Nonlinear Kerr effect; Atmospheric propagation

16. SECURITY CLASSIFICATION OF:			17. LIMITATION OF ABSTRACT	18. NUMBER OF PAGES	19a. NAME OF RESPONSIBLE PERSON
a. REPORT	b. ABSTRACT	c. THIS PAGE			Phillip Sprangle
Unclassified	Unclassified	Unclassified	UL	62	19b. TELEPHONE NUMBER *(include area code)* (202) 767-3493

Standard Form 298 (Rev. 8-98)
Prescribed by ANSI Std. Z39.18

Ultrashort Laser Pulses and Electromagnetic Pulse Generation in Air and on Dielectric Surfaces

Phillip Sprangle, Joseph Peñano, Bahman Hafizi[1] and C. A. Kapetanakos[2]

Naval Research Laboratory

Plasma Physics Division, Washington, DC 20375

Abstract

Intense, ultrashort laser pulses propagating in the atmosphere have been observed to emit sub-THz electromagnetic pulses (EMP). The purpose of this paper is to analyze EMP generation from the interaction of ultrashort laser pulses with air and with dielectric surfaces and to determine the efficiency of conversion of laser energy to EMP energy. In our self-consistent model the laser pulse partially ionizes the medium, forms a plasma filament, and through the ponderomotive forces associated with the laser pulse, drives plasma currents which are the source of the EMP. The propagating laser pulse evolves under the influence of diffraction, Kerr focusing, plasma defocusing, and energy depletion due to electron collisions and ionization. Collective effects and recombination processes are also included in the model. The duration of the EMP in air, at a fixed point, is found to be a few hundred femtoseconds, i.e., on the order of the laser pulse duration plus the electron collision time. For steady state laser pulse propagation the flux of EMP energy is non-radiative and axially directed. Radiative EMP energy is present only for non-steady state or transient laser pulse propagation. The analysis also considers the generation of EMP on the surface of a dielectric on which an ultrashort laser pulse is incident. For typical laser parameters, the power and energy conversion efficiency from laser radiation to EMP radiation in both air and from dielectric surfaces is found to be extremely small, $< 10^{-8}$. Results of full scale, self-consistent, numerical simulations of atmospheric and dielectric surface EMP generation are presented. A recent experiment on atmospheric EMP generation is also simulated.

[1]Icarus Research, Inc. P.O. Box 30780, Bethesda, MD 20824-0780

[2]LET Corp., 4431 MacArthur Blvd. Washington DC 20007

Contents

I. Introduction 3

II. Electromagnetic Pulse Generation in Air 5

a) Driving Laser Pulse 6

i) Plasma Current 7

ii) Laser Pulse Amplitude 10

iii) Source Dependent Expansion Analysis of Laser Pulse 11

iv) Pulse Group Velocity 12

b) EMP Equations in Air 13

c) Analysis of EMP in Air 14

i) Estimate of EMP Power Conversion Efficiency 16

ii) EMP in the Steady State Regime 18

iii) EMP in the Transient Regime 21

III. EMP Generated on the Surface of a Dielectric 22

IV. Numerical Simulations of EMP Generation 26

a) EMP Generation in Air 27

i) Steady State Laser Pulse Propagation 27

ii) Transient Laser Pulse Propagation 29

iii) Comparison with Experiment 31

iv) High Energy Laser Pulse 33

b) Dielectric Surface Generation 34

V. Summary 36

References 37

I. Introduction

Propagation of intense, ultrashort laser pulses in the atmosphere has demonstrated a wide range of phenomena that may have a variety of applications. The observations include formation and stable, long-distance propagation of optical and plasma filaments, 'white' light generation and emission of sub-THz electromagnetic pulses (EMP) [1-18]. Terahertz radiation has a wide range of applications in areas such as chemical identification, biomedical diagnostics and dielectric measurements. In addition, tomographic imaging using THz radiation has potential applications in biomedical research, security screening and remote sensing. Terahertz radiation is also generated by backward wave oscillators [19], gyrotrons [20], free-electron lasers [21], difference-frequency mixing in nonlinear media [22], photoconductive switches [23], tunable optical parametric oscillators[24], semiconductor lasers [25], optically-pumped THz lasers [26], DC to AC converters [27] and Cherenkov wakes in magnetized plasmas [28].

Recently, it has been observed that a broadband electromagnetic pulse (EMP) of terahertz radiation can be generated within the plasma filaments formed by an ultra-short ($\sim$ 100 fsec), high-intensity ($\sim 10^{13}$-10^{14} W/cm^2) laser pulse propagating in air [14, 17]. In these experiments the laser pulse was sufficiently intense to create a plasma filament through multiphoton ionization of air. The plasma density within the filament was observed to be $\sim 10^{16}$ cm^{-3}. This density corresponds to a plasma wavelength of $\sim 330\,\mu m$ and a plasma frequency of $\sim$ 0.9 THz.

In this paper we analyze and numerically simulate the EMP produced by the interaction of ultrashort laser pulses with air and dielectric surfaces, and determine the conversion efficiency from the laser pulse energy to EMP. Atmospheric EMP is generated when a short, intense laser pulse ionizes the air and forms a plasma filament. The plasma filament extends behind and its front travels with the laser pulse as indicated in Fig. 1. The duration of the plasma current which drives the EMP is limited by the electron collision frequency. For a plasma density of $n_e \sim 10^{16}$ cm^{-3}, the electron collision frequency is $\nu_e \sim 5\times10^{12}$ sec^{-1} (for T_e = 1eV) and the duration of the plasma current is $\sim 1/\nu_e \sim 200$ fsec. The duration of the EMP in air, at a fixed point, is a few hundred femtoseconds, i.e., the laser pulse duration plus the electron collision time. The

spatial gradients associated with the laser pulse envelope as well as electron collisions lead to ponderomotive forces on the plasma electrons. These forces cause the electrons to oscillate, setting up plasma currents. The axial and transverse components of plasma current pulse have velocities close to the group velocity of the laser pulse. This is similar to the laser driven excitation of plasma waves in the laser wakefield accelerator (LWFA) [29]. In the LWFA plasma oscillations occur at the local plasma frequency. In general the various field components of the plasma oscillations are coupled, as are the axial and transverse plasma currents. These induced plasma currents, which travel with the laser pulse, are the source of the atmospheric EMP. The axial extent of the EMP is limited, and consequently, the spectrum of the EMP pulse can be broad. However, the characteristic frequency of the EMP measured outside of the plasma filament is determined by the laser pulse duration and not the local plasma frequency.

The results of our analysis for atmospheric EMP generation can be summarized as follows. For steady state propagation, in which the laser pulse and plasma filament are static in the group velocity frame of the laser pulse, the plasma current source travels with a velocity equal to the laser pulse group velocity. Since the group velocity is necessarily less than the speed of light, there is no EMP radiation generated. The absence of radial EMP emission in the steady state is one of several fundamental differences between our results and those of Refs. [30] and [31], see also [32]. The absence of EMP in the steady state is analogous to the lack of Cherenkov radiation when the velocity of a charged particle is less than the velocity of light in the medium. The radial component of the plasma current in the filament can lead to surface charges on the plasma-air boundary. The surface charge density is strongly dependent on the collisionality of the plasma. In the weakly collisional regime the surface charge leads to greatly reduced EMP fields beyond the filament.

Under conditions of non-steady state (transient) propagation, the plasma currents can generate EMP having a radial energy flux. For non-steady state pulse propagation, the plasma currents can have Fourier components with phase velocities greater than the laser pulse group velocity. These Fourier components can generate radiative EMP, analogous to Cherenkov radiation. A condition for generating radiative EMP in the transient regime is derived and the differing characteristics of EMP in the steady state and

transient propagation regimes are discussed in detail and illustrated with simulations. For typical atmospheric conditions and laser parameters it is found that the efficiency of the EMP generation from laser-atmospheric interaction, i.e., the ratio of the EMP energy to the laser pulse energy, is extremely small.

In addition to atmospheric EMP generation we consider EMP from the interaction of short laser pulses with dielectric surfaces. The source of the EMP on the surfaces of the dielectric is the oscillating plasma sheet formed by the ionization process as well as an optical rectification process. Our analysis of EMP generation on the surfaces of a dielectric indicates that the conversion efficiency is extremely small.

This paper is organized as follows. The general equations describing the evolution of the driving laser pulse and EMP in air are derived in Sec. II. Also in Sec. II, an estimate of the EMP power conversion efficiency is derived and an analysis of the steady state and transient propagation regimes presented. In Sec. III EMP generation from a dielectric surface on which a laser pulse is incident is analyzed. Section IV presents self-consistent numerical simulations showing laser pulse propagation, plasma filament formation, and EMP generation in air and on dielectric surfaces. A summary of the results and concluding remarks are found in Sec. V.

II. Electromagnetic Pulse Generation in Air

In this section we derive the general equations for the generation of EMP radiation from laser-induced plasma currents in air. For the parameters of interest, the driving laser pulse intensity is sufficiently high that it partially ionizes the air and forms a plasma filament behind the laser pulse. An equation for the amplitude of the driving laser pulse is derived that includes the effects of diffraction, Kerr focusing, plasma defocusing, electron collisions and laser pulse energy depletion caused by ionization. The plasma currents within the filament are driven by the ponderomotive forces associated with the laser pulse and are described by a set of cold fluid equations which include the effects of multi-photon ionization, electron-neutral elastic collisions and electron recombination/attachment. In our model an axially symmetric laser-plasma configuration is assumed and stimulated Raman scattering of the laser pulse and other instabilities are not considered [33, 34].

a) Driving Laser Pulse

For a self-consistent description of EMP generation the spatial and temporal evolution of the driving laser pulse is needed. The ponderomotive forces, which are proportional to the energy density of the driving laser pulse, induce low frequency plasma currents which in turn generate EMP. The driving laser pulse is assumed to be many optical wavelengths long and to have a spot size that is large compared to the wavelength. The transverse laser fields are given by

$$\mathbf{E}_L(\mathbf{r},t) = E_L(\mathbf{r},t)\exp(\, i(k_0 z - \omega_o t))\hat{\mathbf{e}}_x / 2 + c.c., \tag{1a}$$

$$\mathbf{B}_L(\mathbf{r},t) = B_L(\mathbf{r},t)\exp(i(k_0 z - \omega_o t))\hat{\mathbf{e}}_y / 2 + c.c., \tag{1b}$$

where ω_o is the carrier frequency, $k_o = \omega_o / c$ is the wavenumber, $\hat{\mathbf{e}}_x$ ($\hat{\mathbf{e}}_y$) is a unit vector in the x (y) direction and c.c. denotes the complex conjugate. In Eq.(1a) E_L is the slowly varying complex electric field amplitude satisfying $\left|E_L^{-1}\,\partial E_L / \partial t\right| << \omega_o$ and $\left|E_L^{-1}\,\partial E_L / \partial z\right| << k_o$. The transverse magnetic field amplitude is $B_L \cong [1 - i(c/\omega_0)(\partial/\partial z + c^{-1}\partial/\partial t)]E_L$. The axial electric and magnetic fields of magnitude $\sim(c/\omega_o)\left|\partial E_L / \partial x\right|$ and $\sim (c/\omega_o)\left|\partial E_L / \partial y\right|$, respectively, that are associated with the transverse laser fields in Eqs.(1), are small and are neglected.

Making use of the electron cold fluid equations, the transverse current density $\mathbf{J}_L = q\, n_e\, \mathbf{v}_L$ induced by the laser pulse is given by

$$\frac{\partial \mathbf{J}_L}{\partial t} + \nu_e \mathbf{J}_L = \frac{\omega_p^2(\mathbf{r},t)}{4\pi}\mathbf{E}_L, \tag{2}$$

where $\nu_e = \nu_{en} + \nu_{ei}$ is the electron collision frequency, ν_{en} is the electron-neural collision frequency, ν_{ei} is the electron-ion collision frequency, $\omega_p(\mathbf{r},t) = (4\pi q^2\, n_e(\mathbf{r},t)/m)^{1/2}$ is the local plasma frequency, q is the electronic charge, $\mathbf{v}_L$ is the quiver velocity in the laser field and n_e is the electron density in the plasma filament which is formed by photoionization. It is assumed that the ions are immobile on the time scale of interest. In general, the electron density n_e includes contributions from

plasma oscillations as well as the ionization process. The solution of Eq.(2) for the first order transverse current density induced by the laser field is

$$\mathbf{J}_L(\mathbf{r},t) = J_L(\mathbf{r},t)\exp(i(k_o z - \omega_o t))\hat{\mathbf{e}}_x/2 + c.c., \qquad (3)$$

where $J_L \cong (i/4\pi\omega_o)[1-(i/\omega_o)(\partial/\partial t + \nu_e)](\omega_p^2 E_L)$, where we have assumed that $\omega_o >> \nu_e$.

The electron-neutral collision frequency is given by $\nu_{en} = n_n \sigma_0 (k_B T_e/m)^{1/2}$ where $n_n = n_{no} - n_e$ is the neutral density (singly ionized plasma), n_{no} is the ambient neutral density, k_B is the Boltzmann constant and $\sigma_0 \approx 5\times10^{-15}$ cm^2 is a typical value for the scattering cross section [35]. In practical units the expression can be written as $\nu_{en}[\sec^{-1}] \approx 2\times10^{-7}\, n_n[\mathrm{cm}^{-3}](T_e[\mathrm{eV}])^{1/2}$. For a neutral air density of $n_n = n_{no} = 2.7\times10^{19}$ cm^{-3} and temperature $T_e = 1$eV, the electron collision frequency is $\nu_{en} \approx 5.7\times10^{12}$ sec^{-1}. Note that for a plasma density of $n_e \sim 10^{16}$ cm^{-3}, the electron-neutral collision frequency and plasma frequency are comparable, $\nu_{en} \sim \omega_p$. Taking the Coulomb logarithm to be equal to 10, the electron-ion collision frequency [35] is $\nu_{ei}[\sec^{-1}] \approx 3\times10^{-5}\, n_i[\mathrm{cm}^{-3}](T_e[\mathrm{eV}])^{-3/2}$, for singly ionized plasma, i.e., $n_e = n_i$. The electron-neural and electron-ion collision frequency become equal when the electron density reaches the value $n_e \approx 1.8\times10^{17}\, T_e^2[eV]$ for singly ionized plasma.

i) Plasma Current

The propagation of the driving laser pulse is strongly influence by the plasma filament. The plasma dynamics are described by the non-relativistic, cold fluid equations

$$\frac{\partial n_e}{\partial t} + \nabla\cdot(n_e\,\mathbf{v}) = \nu_{ion}\, n_n - \beta_{recom}\, n_e^2 - \beta_{attach}\, n_e\, n_n^2, \qquad (4a)$$

$$\frac{\partial \mathbf{v}}{\partial t} + (\mathbf{v}\cdot\nabla)\mathbf{v} = \frac{q}{m}\left(\mathbf{E} + \frac{\mathbf{v}\times\mathbf{B}}{c}\right) - \nu_e\,\mathbf{v} - \left(\frac{\partial n_e}{\partial t} + \nabla\cdot(n_e\,\mathbf{v})\right)\mathbf{v}/n_e, \qquad (4b)$$

where, $\mathbf{v}$ is the electron fluid velocity, ν_{ion} is the ionization rate, β_{recom} is the recombination coefficient, β_{attach} is the attachment coefficient, $n_n = n_{no} - n_e$, $\nu_e = \nu_{en} + \nu_{ei}$ and the ions are assumed to be stationary. In obtaining Eq.(4) we have

assumed that the electrons immediately after ionization have zero velocity, i.e., the electrons are born at rest and above threshold ionization effects are ignored.

For the parameters of interest here the ionization process is principally due to multi-photon ionization and the corresponding rate can be fitted analytically by [36]

$$\nu_{ion} = \frac{2\pi\,\omega_o}{(\ell-1)!}\left(\frac{I_L(r,z,t)}{I_{MP}}\right)^{\ell}, \tag{5}$$

where the integer $\ell \le Int(U_{ion}/\hbar\omega_o + 1)$ refers to the effective number of photons absorbed by the molecule in the ionization process, U_{ion} is the ionization energy, I_L is the laser intensity and $I_{MP} = \hbar\omega_o^2/\sigma_{MP}$, with σ_{MP} an empirically determined ionization cross section. At laser intensities of $\sim 10^{14}$ W/cm^2 or above tunneling ionization becomes important. For a laser wavelength of $\lambda_o = 0.8\,\mu\text{m}$ ($\hbar\omega_o = 1.54\,\text{eV}$) in air, the multi-photon ionization order of O_2 is $\ell = 8$, and the characteristic intensity is determined empirically to be $I_{MP} \sim 10^{14}$ W/cm^2 for pulses with durations $\sim$ 100 fsec [16]. Since the intensity ratio in Eq.(5) is raised to the eighth power, the ionization rate is an exceedingly sensitive function of the laser intensity and the value of the parameter I_{MP}. The scaling of the ionization rate in Eq.(5) with laser intensity is the same as that given in Ref. [37]. Since the numerical value of the Keldysh formula in [37] differs from the experimental value, we use the empirical cross-section quoted above. A similar approach was adopted in Ref. [38] to obtain an empirical formula for the multi-photon ionization rate. For a laser intensity of $I_L = 7\times10^{13}$ W/cm^2, laser wavelength of $\lambda_o = 0.8\,\mu m$ ($\omega_o = 2.4\times10^{15}\,\text{sec}^{-1}$) and ionization order of $\ell = 8$, the ionization rate is $\nu_{ion} \sim 2\times10^{11}\,\text{sec}^{-1}$. The ionization rate, however, is an extremely sensitive function of the laser intensity. The recombination time is given by $\tau_{recom} = 1/\beta_{recom}\,n_e$. Taking $\beta_{recom}\,[\text{cm}^3/\text{sec}] \approx 2\times10^{-8}\,(T_e[\text{eV}])^{-1/2}$ [14], $n_e = 10^{16}$ cm^{-3}, and $T_e = 1\,\text{eV}$, the recombination time $\tau_{recom} \sim 5\,\text{nsec}$ The attachment coefficient β_{attach} of electrons on oxygen molecules is discussed in Ref [39]. For an electron temperature of $\sim$ 1 eV the attachment coefficient is $\beta_{attach} \sim 3.4\times10^{-31}$ cm^6/sec and the attachment time is

$\tau_{attach} = 1/\beta_{attach}\, n_n^2 \sim 4\,\text{nsec}$. The duration of the plasma filament is on the order of the shorter of the two times scales, τ_{recom} and τ_{attach}, i.e., $\min[\tau_{recom}, \tau_{attach}]$.

Combining Eqs.(4a) and (4b) results in an equation for the electron plasma current density, $\mathbf{J} = q\, n_e \mathbf{v}$, given by [40]

$$\frac{\partial \mathbf{J}}{\partial t} + \nu_e \mathbf{J} = \frac{\omega_p^2}{4\pi}\mathbf{E} + \mathbf{S} \quad , \tag{6}$$

where $\mathbf{S}(r,z,t)$ is the nonlinear driving term. The first term on the right-hand-side of Eq.(6) is associated with collective effects while the second term represents the driving ponderomotive force due to the laser pulse. The duration of the plasma current density is limited to $\sim 1/\nu_e \sim 200\,\text{fsec}$ for $n_e = 10^{16}\ \text{cm}^{-3}$. To second order in the laser field amplitude,

$$\mathbf{S} = \frac{q}{mc}\mathbf{J}_L \times \mathbf{B}_L - q^{-1}(\nabla \cdot \mathbf{J}_L)\mathbf{J}_L / n_e - q^{-1}(\mathbf{J}_L \cdot \nabla)(\mathbf{J}_L / n_e). \tag{7}$$

When the laser spot size is large compared to the plasma filament spot size, i.e., $R_o >> r_p$, the ponderomotive source term in Eq.(7) can be simplified. This is a valid approximation in the case of higher order multi-photon ionization where the ionization rate is a strong function of laser intensity. In this limit the axial component of the source term S_z is given by

$$S_z(r,z,t) \approx -\frac{q}{16\pi m}\frac{\omega_p^2(r,z,t)}{\omega_o^2}\left(\frac{\partial}{\partial z} - \frac{2\nu_e}{c} - \frac{2}{c\,\omega_p^2}\frac{\partial \omega_p^2}{\partial t}\right)\left|E_L(r,z,t)\right|^2. \tag{8}$$

Note that the axial ponderomotive force consists of a contribution from the spatial gradient of the laser pulse envelope as well as contributions from electron collisions and changes in the electron density (ionization). The transverse component of the source term, for the laser pulse linearly polarized in the x direction, is

$$\mathbf{S}_\perp \approx -\frac{q}{16\pi m}\frac{\omega_p^2(r,z,t)}{\omega_o^2}\left(\hat{\mathbf{e}}_r \frac{\partial}{\partial r} + \hat{\mathbf{e}}_x \frac{2}{\omega_p^2}\frac{\partial \omega_p^2}{\partial x}\right)\left|E_L(r,z,t)\right|^2, \tag{9}$$

where $\hat{\mathbf{e}}_r$ is a unit vector in the radial direction. Note that the transverse part of the source term has a component in the x direction. For a circularly polarized laser pulse the

axial component of the source term is given by Eq.(8) with E_L replaced with $\sqrt{2}E_L$ and the transverse component is purely radial and given by

$$\mathbf{S}_\perp \approx -\frac{q}{8\pi m}\frac{\omega_p^2(r,z,t)}{\omega_o^2}\left(\frac{\partial}{\partial r}+\frac{1}{\omega_p^2}\frac{\partial \omega_p^2}{\partial r}\right)\left|E_L(r,z,t)\right|^2\hat{\mathbf{e}}_r. \qquad (10)$$

The axially symmetric circularly polarized laser field has been assumed to be of the form $\mathbf{E}_L = E_L \exp(i(k_o z-\omega_o t))(\hat{\mathbf{e}}_x - i\hat{\mathbf{e}}_y)/2 + c.c.$

ii) Laser Pulse Amplitude

To obtain the ponderomotive source term self consistently, an equation describing the evolution of the driving laser pulse is needed. For this purpose it is useful to transform to the group velocity frame in which the independent variables are z and $\tau = t - z/\mathrm{v}_g$ where v_g denotes the linear group velocity of the laser pulse, and is defined later. In terms of the new independent variables (z,τ) the derivatives are given by $\partial/\partial t \to \partial/\partial\tau$ and $\partial/\partial z \to \partial/\partial z - \mathrm{v}_g^{-1}\partial/\partial\tau$. In the variables (z,r,τ) the laser pulse evolves slowly, i.e., is nearly stationary. The wave equation for the complex laser amplitude $E_L(r,z,\tau)$ in the new independent variables takes the form [36]

$$\frac{\partial E_L(r,z,\tau)}{\partial z} = \frac{i}{2}\frac{c}{\omega_o}\left(\nabla_\perp^2 + \frac{\omega_o^2 n_K}{4\pi c}\frac{n_n}{n_{no}}\left|E_L\right|^2 - \frac{\omega_{po}^2(r,z,\tau)}{c^2}\left(1-i\frac{\nu_e}{\omega_o}\right)\right.$$
$$\left. + 8\pi i\frac{\omega_o}{c^2}\frac{U_{ion}}{\left|E_L\right|^2}\frac{\partial n_{eo}}{\partial\tau}\right)E_L(r,z,\tau). \qquad (11)$$

The first term on the right hand side of Eq.(11) is the Laplacian operator which is responsible for diffractive spreading of the laser beam. The second term is proportional to the nonlinear Kerr refractive index n_K and can lead to nonlinear self-focusing [40, 41]. The terms proportional to ω_{po}^2 represent the effect of plasma defocusing and collisions [36, 40]. The last term describes laser pulse energy depletion due to ionization of the air molecules with effective ionization energy U_{ion}. In general the refractive index for electromagnetic waves in a medium consists of contributions from the linear and nonlinear polarization field. In the present analysis it is assumed that the contribution to the nonlinear refractive index is proportional to the laser intensity, i.e., Kerr effect. This

is a valid approximation for in a gas as well as for an amorphous dielectric. For the laser pulse this nonlinear contribution to the index leads to the phenomena of nonlinear Kerr self focusing.

iii) Source Dependent Expansion Analysis of Laser Pulse

Equation (11) for the laser pulse amplitude can be approximately solved by employing the source dependent expansion (SDE) method [42]. In this method the laser field is assumed to have a Gaussian transverse profile

$$\left|E_L(r,z,\tau)\right| = \left|E_L(0,z,\tau)\right| \exp(-r^2/R^2(z,\tau)), \tag{12}$$

where R is the laser spot size. For the Gaussian transverse profile the laser power is

$$P_L(z,\tau) = c\left|E_L(0,z,\tau)\right|^2 R^2(z,\tau)/16. \tag{13}$$

Employing the SDE method results in coupled equations for the spot size and power,

$$\frac{\partial^2 R(z,\tau)}{\partial z^2} - \frac{4c^2}{\omega_o^2}\frac{1}{R^3(z,\tau)}\left(1 - \frac{P_L(z,\tau)}{P_K} + \frac{2\pi\ell r_e n_{eo}(0,z,\tau)}{(\ell+1)^2}R^2(z,\tau)\right) = W(z,\tau), \tag{14a}$$

$$\frac{\partial P_L(z,\tau)}{\partial z} = -\frac{1}{\ell+1}\frac{\omega_{po}^2(0,z,\tau)}{\omega_o^2}\frac{\nu_e}{c}P_L(z,\tau) - \frac{\pi}{2\ell}U_{ion}\nu_{ion}n_n R^2(z,\tau), \tag{14b}$$

where $P_K = \lambda_o^2/(2\pi n_K n_n/n_{no})$ is the nonlinear Kerr focusing power, $r_e = q^2/mc^2$ is the classical electron radius and

$$W(z,\tau) = -\frac{1}{R}\left(\frac{\partial}{\partial z}\left(R^2 U\right) + R^2 U^2\right), \tag{15a}$$

$$U(z,\tau) = \frac{(\ell-1)}{2\ell}\frac{1}{P_L}\frac{\partial P_L}{\partial z} - \frac{1}{2\ell(\ell+1)^2}\frac{\omega_{po}^2}{\omega_o^2}\frac{\nu_e}{c}, \tag{15b}$$

$$\frac{\partial n_{eo}}{\partial \tau} = \nu_{ion} n_n. \tag{15c}$$

The decrease in the total laser pulse power as a function of propagation distance is due to both collisional absorption and ionization. The evolution of the total laser pulse power given by Eq.(14b) can be rewritten as

$$\frac{\partial P_L(z,\tau)}{\partial z} = -\left(\frac{1}{L_{coll}} + \frac{1}{L_{ion}}\right)P_L(z,\tau), \tag{16}$$

where

$$L_{coll} = (\ell+1)\frac{\omega_o^2}{\omega_{po}^2}\frac{c}{\nu_e}, \tag{17a}$$

is the absorption length due to collisional effects and

$$L_{ion} = \frac{2\ell}{\pi}\frac{P_L}{U_{ion}\,\nu_{ion}\,n_n R^2}, \tag{17b}$$

is the absorption length due to ionization effects. It should be noted that due to the nonlinear character of Eq.(16), the expressions in Eqs.(17) are at best local estimates for the scale lengths. As an example, consider the case of a laser pulse having a power $P_L = 0.1\text{TW}$, wavelength $\lambda_o = 0.8\,\mu m$, pulse duration $\tau_L = 100\,\text{fsec}$, intensity $I_L = 5\times10^{13}\ \text{W/cm}^2$ and spot size $R \sim 360\,\mu m$, propagating in air with a neutral density $n_{no} = 2.7\times10^{19}\ \text{cm}^{-3}$, effective ionization energy of $U_{ion} = 8\,\text{eV}$ $(\ell = 8)$ and electron collision frequency of $\nu_e = \nu_{en} + \nu_{ei} \approx 6\times10^{12}\ \text{sec}^{-1}$. In this case the ionization rate is $\nu_{ion} \sim 10^{10}\ \text{sec}^{-1}$ $(I_{MP} = 10^{14}\ \text{W/cm}^2)$ and the electron density is $n_e \sim 3\times10^{16}\ \text{cm}^{-3}$, $(\omega_o/\omega_{po} \sim 230)$. For these parameters the collisional absorption length is $L_{coll} \sim 25\,\text{m}$ while the ionization absorption length is $L_{ion} \sim 10\ \text{m}$. In this example, the laser pulse propagation distance is limited by ionization absorption. It should be stressed that these characteristic scale lengths are very sensitive functions of the laser and plasma parameters.

iv) Pulse Group Velocity

The group velocity is given by $\text{v}_g = c(n + \omega_o\,\partial n/\partial\omega_o)^{-1}$, where n is the total refractive index and expressible as

$$n \cong n_o - \frac{f\,\omega_{po}^2}{2\omega_o^2} - \frac{2c^2}{\omega_o^2 R_o^2} + n_K I_L. \tag{18}$$

Here R_o is the initial spot size of the laser pulse, and $I_L = c\,n_o|E_L|^2/8\pi$ is the time-averaged laser intensity. The filling factor f is the ratio of the plasma filament cross sectional area to the laser pulse cross sectional area. Using the expression for the plasma density due to the multi-photon ionization process in Eq.(5) we find that $f \sim (\ell+1)^{-1}$. The filling factor is necessary for calculating the correct group velocity of the laser pulse

in the presence of the plasma filament. The third term on the right hand side of Eq.(18) denotes the correction to the refractive index due to the finite spot size of the laser pulse and the fourth term represents the nonlinear index due to the Kerr effect. Making use of the expression for the refractive index, the group velocity $v_g = c\beta_g = 1/(n+\partial(\omega_o n)/\partial\omega_o)$ is expressible as

$$\beta_g \cong \frac{1}{n_o} - \frac{f\omega_{po}^2}{2\omega_o^2} - \frac{2c^2}{\omega_o^2 R_o^2} - n_K I_L . \tag{19}$$

In deriving Eq.(19), it is assumed that the variation of the linear index and Kerr index with frequency is negligible. For $I_L = 10^{14}$ W/cm^2, $R_o = 260\mu m$, $\lambda_o = 0.8\mu$m, $n_e = 10^{16}$ cm^{-3}, $n_K = 6\times10^{-19}$ cm^2/W, and $\ell = 8$, the magnitudes of the plasma, finite spot size, and optical Kerr contributions to β_g are, $\sim 3\times10^{-7}$, 3×10^{-6}, and $\sim 6\times10^{-5}$, respectively.

b) EMP Equations in Air

The wave equation for the EMP electric field **E** in air which is driven by plasma currents is given by

$$\nabla\times\nabla\times\mathbf{E} + \frac{n_o^2}{c^2}\frac{\partial^2\mathbf{E}}{\partial t^2} = -\frac{4\pi}{c^2}\frac{\partial\mathbf{J}}{\partial t}, \tag{20}$$

where n_0 is the linear refractive index and the plasma current is given by Eq.(6). We use a cylindrical coordinate system where r, θ, and z denote the radial coordinate, azimuthal angle, and axial coordinate, respectively, and assume axial symmetry, i.e., $\partial/\partial\theta = 0$. The generation of EMP from the surface of dielectrics is analyzed in Sec. III. In the laser pulse group velocity frame, the axial and radial components of the EMP electric field are given by

$$\left(\frac{1}{r}\frac{\partial}{\partial r}\left(r\frac{\partial}{\partial r}\right) - \frac{1}{c^2}\frac{\partial^2}{\partial\tau^2}\right)E_z + \left(\frac{1}{v_g}\frac{\partial}{\partial\tau} - \frac{\partial}{\partial z}\right)\frac{1}{r}\frac{\partial}{\partial r}(rE_r) = \frac{4\pi}{c^2}\frac{\partial J_z}{\partial\tau}, \tag{21a}$$

$$\left(\frac{1}{v_g^2\gamma_g^2}\frac{\partial^2}{\partial\tau^2} - \frac{2}{v_g}\frac{\partial^2}{\partial z\partial\tau} + \frac{\partial^2}{\partial z^2}\right)E_r + \left(\frac{1}{v_g}\frac{\partial}{\partial\tau} - \frac{\partial}{\partial z}\right)\frac{\partial E_z}{\partial r} = \frac{4\pi}{c^2}\frac{\partial J_r}{\partial\tau}, \tag{21b}$$

where $\gamma_g \equiv (1 - n_0^2 v_g^2/c^2)^{-1/2}$. Using Eq.(19) γ_g is found to be given by

$$\gamma_g \cong \omega_o / \left(f\,\omega_{po}^2 + 4c^2/R_o^2 + 2\omega_o^2 n_K I_L \right)^{1/2}. \qquad (22)$$

For $\lambda_o = 0.8\mu m$, $n_e = 10^{17}$ cm^{-3}, $n_K = 6\times10^{-19}$ cm^2/W, $I_L = 10^{14}$ W/cm^2, $\ell = 8$, and $R_o = 260\mu m$, we find that the plasma wavelength $\lambda_p = 2\pi c/\omega_p \sim 106\mu m$ and $\gamma_g \approx 90$.

Taking the Fourier transform of Eqs.(21a, b) together with Eq.(6) in the variables z and τ, with the convention $Q = (2\pi)^{-1}\int_{-\infty}^{\infty}\tilde{Q}\exp(ikz - i\omega\tau)\,dk\,d\omega$, gives

$$\left(\frac{1}{r}\frac{\partial}{\partial r}\left(r\frac{\partial}{\partial r}\right) + \frac{\omega^2}{c^2} - \frac{\omega_p^2(r)}{c^2(1+i\nu_e/\omega)} \right)\tilde{E}_z - i\left(\frac{\omega}{v_g} + k \right)\frac{1}{r}\frac{\partial}{\partial r}\left(r\tilde{E}_r \right) = \frac{4\pi}{c^2}\frac{\tilde{S}_z(r,k,\omega)}{1+i\nu_e/\omega}, \qquad (23a)$$

$$\left(k^2 + \frac{2k\omega}{v_g} + \frac{\omega^2}{v_g^2\gamma_g^2} + \frac{\omega_p^2(r)}{c^2(1+i\nu_e/\omega)} \right)\tilde{E}_r + i\left(\frac{\omega}{v_g} + k \right)\frac{\partial\tilde{E}_z}{\partial r} = -\frac{4\pi}{c^2}\frac{\tilde{S}_r(r,k,\omega)}{1+i\nu_e/\omega}. \qquad (23b)$$

The azimuthal magnetic field is given by

$$\tilde{B}_\theta = \left(1 - \frac{\omega_p^2(r)}{\omega^2(1+i\nu_e/\omega)} \right)\left(1 + \frac{kv_g}{\omega} \right)^{-1}\tilde{E}_r - \frac{4\pi}{c^2}\left(1 + \frac{kv_g}{\omega} \right)^{-1}\frac{\tilde{S}_r(r,k,\omega)}{1+i\nu_e/\omega}. \qquad (24)$$

In obtaining Eqs.(23) we have set n_o equal to unity. In the following section Eqs.(23) and (24) are solved analytically for an idealized plasma filament.

c) Analysis of EMP in Air

We consider steady state and non-steady state (transient) propagation of the laser pulse for an idealized case that can be solved analytically. The laser pulse envelope is taken to have the form

$$|E_L(0,z,\tau)| = \hat{E}_L(z)\sin(\pi\tau/\tau_L), \qquad (25)$$

for $0 \le \tau \le \tau_L$ and $E_L = 0$ otherwise. The front of the laser pulse is at $\tau = 0$ and the back is at $\tau = \tau_L$. We analyze Eqs.(23) and (24) for the case of an idealized plasma filament with radial extent r_p in which the plasma density is constant for $r < r_p$ and zero for $r > r_p$. It is also assumed that the recombination process is negligible and that the

ionization process is sufficiently rapid that the plasma density does not vary longitudinally within and behind the laser pulse, i.e., ω_p is independent of τ. Under these assumptions, Eqs.(23a) and (23b) can be combined to give equations for the axial field inside $(r < r_p)$ and outside $(r > r_p)$ the plasma filament respectively,

$$\left(\frac{1}{r}\frac{\partial}{\partial r}\left(r\frac{\partial}{\partial r}\right) - \kappa_p^2(\omega,k)\right)\widetilde{E}_z = -\frac{4\pi}{\omega^2(1+i\nu_e/\omega)-\omega_{po}^2}\left(\kappa_p^2(\omega,k)\widetilde{S}_z(r,\omega,k) - (\omega/\mathrm{v}_g + k)\frac{1}{r}\frac{\partial}{\partial r}\left(r\widetilde{S}_r(r,k,\omega)\right)\right), \quad (26a)$$

$$\left(\frac{1}{r}\frac{\partial}{\partial r}\left(r\frac{\partial}{\partial r}\right) - \kappa_o^2(\omega,k)\right)\widetilde{E}_z = 0, \quad (26b)$$

where

$$\kappa_o^2(\omega,k) = \frac{\omega^2}{\mathrm{v}_g^2\gamma_g^2} + \frac{2\omega k}{\mathrm{v}_g} + k^2, \quad (27a)$$

$$\kappa_p^2(\omega,k) = \kappa_o^2(\omega,k) + \frac{\omega_{po}^2}{c^2(1+i\nu_e/\omega)}, \quad (27b)$$

and ω_{po} denotes the constant plasma frequency within the channel. The radial component of the source term, i.e., $\widetilde{S}_r$, can be neglected provided $\omega_{po} r_p / c >> 1$. This is assumed to be the case in writing Eqs.(26) and (27). However, in the numerical simulations the radial source term is not necessarily neglected.

The boundary conditions across the plasma-air interface at $r = r_p$, are the continuity of the axial electric field, $\widetilde{E}_z(r=r_p^-) = \widetilde{E}_z(r=r_p^+)$, and the azimuthal magnetic field $\widetilde{B}_\theta(r=r_p^-) = \widetilde{B}_\theta(r=r_p^+)$. Applying the boundary conditions, the axial electric fields inside and outside the plasma filament are respectively,

$$\widetilde{E}_z(r,\omega,k) = \frac{4\pi\widetilde{S}_z(\omega,k)}{\omega^2(1+i\nu_e/\omega)-\omega_{po}^2}\left(1 - \frac{\kappa_o r_p K_1(\kappa_o r_p)}{D(\omega,k)} I_o(\kappa_p r)\right), \quad (28a)$$

$$\widetilde{E}_z(r,\omega,k) = \frac{4\pi\widetilde{S}_z(\omega,k)}{\omega^2(1+i\nu_e/\omega)}\frac{\kappa_o r_p I_1(\kappa_p r_p)}{D(\omega,k)}\left(\frac{\kappa_0}{\kappa_p}\right)K_o(\kappa_o r), \quad (28b)$$

where I_o and K_o are the modified Bessel functions of order zero of the first and second kind, respectively,

$$D(\omega,k) = h(\omega,k)\kappa_p r_p K_o(\kappa_o r_p) I_1(\kappa_p r_p) + \kappa_o r_p K_1(\kappa_o r_p) I_o(\kappa_p r_p), \qquad (29a)$$

and

$$h(\omega,k) = \left(1 - \frac{\omega_{po}^2}{\omega^2(1 + i\nu_e/\omega)}\right)\frac{\kappa_o^2(\omega,k)}{\kappa_p^2(\omega,k)}. \qquad (29b)$$

Making use of Eqs.(28a) and (28b) the ratio of the field at the boundary to the field at the center of the filament is

$$\frac{\tilde{E}_z(r = r_p)}{\tilde{E}_z(r = 0)} = \frac{h(\omega,k)\kappa_p r_p I_1(\kappa_p r_p) K_o(\kappa_o r_p)}{D(\omega,k) - \kappa_o r_p K_1(\kappa_o r_p)}. \qquad (30)$$

In the plasma filament there is a radial component of plasma current density that induces a surface charge at the plasma-air boundary. The resulting charge distribution is such that the EMP fields outside the filament are extremely small. Neglecting the radial source term $\mathbf{S}_r$ in Eq.(24), continuity of the azimuthal magnetic field across the boundary implies that

$$\frac{\tilde{E}_r(r=r_p^+)}{\tilde{E}_r(r=r_p^-)} = 1 - \frac{\omega_{po}^2}{\omega^2(1 + i\nu_e/\omega)}. \qquad (31)$$

In the weakly collisional regime ($\nu_e << \omega$) and for $\omega \sim \omega_p$ it follows that the field outside is nearly completely shielded. In the highly collisional regime, however, the EMP field is not shielded outside the filament.

In subsections ii) and iii) we analyze and discuss limiting cases of these equations for comparison with the numerical results.

i) Estimate of EMP Power Conversion Efficiency

A rough estimate for the efficiency of converting laser power to EMP power can be obtained by using rather general arguments concerning the EMP field amplitudes. This provides a consistency check with the calculation of efficiency obtained by the far more precise analysis which follows. In addition, this estimate shows that the low efficiencies obtained by more precise analysis are to be expected.

The maximum amplitude of the longitudinal electric field (wakefield) induced by the driving laser pulse propagating in the plasma filament in the absence of collisions is given by [19]

$$E_{z,\max} \approx \frac{\pi^2}{2}\frac{mc^2}{q}\frac{a_L^2}{c\tau_L}, \tag{32}$$

where $a_L = q|E_L|/mc\omega_o$ is the laser strength parameter. The frequency of the wakefield is in the THz range and determined by the laser pulse duration τ_L. In the absence of collisions, the maximum field amplitude occurs when the laser pulse duration is approximately equal to the plasma frequency $\omega_p \tau_L \sim 1$, [29]. The other components of the EMP fields induced by the driving laser pulse are of the same order or smaller than the above maximum axial field. The power in the EMP is estimated to be $P_{EMP} \sim cE_{z,\max}^2 \Sigma/8\pi$ where Σ is the area through which the EMP energy flows. The area of the cylinder enclosing the EMP fields is estimated to be $\Sigma \approx \pi(2N_p r_p c\tau_L + r_p^2)$, where N_p is the number of periods (i.e., plasma wavelengths) of the wakefield behind the laser pulse. The parameter N_p is a measure of the axial extent of the emitting region of the EMP. The driving laser pulse power can be written in terms of the laser strength parameter, $P_L = (c/16)(mc\omega_o R/q)^2 a_l^2$. Using Eq.(32) and the expression for the laser power we find that an estimate for the EMP power efficiency is

$$\eta_{Power} = \frac{P_{EMP}}{P_L} \sim \frac{\pi^2}{8}\left(\frac{a_L\lambda_o}{c\tau_L}\right)^2\left(\frac{2N_p r_p c\tau_L + r_p^2}{R^2}\right), \tag{33}$$

where λ_o is the laser wavelength. As an illustration, consider a laser pulse intensity of $I_L = 7\times10^{13}\,W/cm^2$ and wavelength $\lambda_o = 0.8\,\mu m$, the laser strength parameter for these values is $a_L = 5.7\times10^{-3}$. For a laser pulse length of $\tau_L = 250f\,\mathrm{sec}$, the power efficiency is

$$\eta_{Power} \sim 2\times10^{-8}\left(\frac{2N_p r_p c\tau_L + r_p^2}{R^2}\right). \tag{34}$$

Taking the laser spot to be $R = 200\,\mu m$, plasma filament spot size to be $r_p = 100\,\mu m$, number of plasma wavelengths behind the pulse to be $N_p \sim 10$, the efficiency is extremely small, $\eta_{Power} \sim 10^{-7}$. This estimate is typical of the values obtained by numerically solving the full set of EMP equations.

ii) EMP in the Steady State Regime

In the steady state propagation regime it is assumed that both the plasma density and the laser pulse are independent of the propagation distance, i.e., $\partial \omega_{po}^2 / \partial z = \partial \left|\hat{E}_L\right|^2 / \partial z = 0$. Even in a homogeneous medium there is a minimum propagation distance needed to reach a steady state. The steady state EMP propagates with velocity equal to the phase velocity of the laser pulse, v_g. The transient EMP on the other hand propagates with velocity $\sim c/n_o$. The propagation distance needed to reach a steady state is $L_{steady-state} \sim \tau_L / \left|1/v_g - n_o/c\right| \sim 2\gamma_g^2 c\tau_L$. For the purpose of illustration it will be assumed that the collision frequency can be neglected.

The axial EMP electric field is vanishingly small outside of the plasma filament, while inside the filament it is given by

$$\tilde{E}_z(r,\omega) = \frac{4\pi \tilde{S}_z(\omega)}{\omega^2 - \omega_{po}^2}\left(1 - \frac{I_o(\kappa_p r)}{I_o(\kappa_p r_p)}\right). \tag{35}$$

The EMP magnetic field inside and outside of the plasma filament is given by

$$\tilde{B}_\theta(r,\omega) = \frac{4\pi i}{\omega}\frac{\tilde{S}_z(\omega)}{c\kappa_p}\frac{I_1(\kappa_p r)}{I_o(\kappa_p r_p)}, \tag{36a}$$

and

$$\tilde{B}_\theta(r,\omega) = \frac{4\pi i}{\omega}\frac{\tilde{S}_z(\omega)}{c\kappa_p}\frac{I_1(\kappa_p r_p)}{I_o(\kappa_p r_p)}\frac{K_1(\kappa_o r)}{K_1(\kappa_o r_p)}, \tag{36b}$$

respectively. For typical parameters we find that $\kappa_p r_p \sim \omega_{po} r_p / c >> 1$ and $\kappa_o r_p \sim \omega r_p/(c\gamma_g) << 1$ and the EMP magnetic field inside and outside the plasma filament reduces to

$$\tilde{B}_\theta(r,\omega) = \frac{4\pi i}{\omega}\frac{\tilde{S}_z(\omega)}{c}\left(\frac{2\pi c r_p}{\omega_{po}}\right)^{1/2} \exp(-\omega_{po} r_p / c) I_1(\omega_{po} r / c), \quad (37a)$$

$$\tilde{B}_\theta(r,\omega) = \frac{4\pi i \tilde{S}_z(\omega)}{\omega_{po}}\frac{r_p}{v_g \gamma_g} K_1(\omega r / v_g \gamma_g). \quad (37b)$$

In the steady state and in the absence of collisions the Fourier transform of the source term in Eq.(8) is

$$\tilde{S}_z(\omega) = -\frac{iq}{2mc}\frac{\omega}{c}\frac{\omega_{po}^2}{\omega_o^2}\tilde{I}_L(\omega), \quad (38)$$

where $I_L(\tau) = c|E_L|^2/8\pi$ is the laser intensity.

To obtain the temporal variation of the fields it is necessary to invert the corresponding Fourier transforms. To derive an analytic expression for $B_\theta(r,\tau)$ we assume an intensity profile $I_L(\tau) = I_{L0}$ for $0 < \tau < \tau_L$ and zero otherwise. Substituting Eq.(38) into Eq.(36) and taking the inverse Fourier transform results in

$$B_\theta(r,\tau) = B_o \frac{r_p}{r} H(r,\tau), \quad (39)$$

where

$$H(r,\tau) = \frac{1}{2}\left(\frac{\tau}{\left((r/v_g\gamma_g)^2 + \tau^2\right)^{1/2}} - \frac{(\tau - \tau_L)}{\left((r/v_g\gamma_g)^2 + (\tau-\tau_L)^2\right)^{1/2}}\right), \quad (40a)$$

and

$$B_o = \frac{2\pi q}{mc^2}\frac{\omega_{po}}{\omega_o^2} I_{L0}. \quad (40b)$$

is the peak magnetic field at $r = r_p$ and $\tau = \tau_L$. Note that the magnetic field in Eq.(39) is proportional to the square root of the plasma density. This dependence is due to the near-cancellation of the axial components of the convective and inductive current densities. Evaluating the magnetic field at $r = r_p$ in Eq.(37a) and noting that $\omega_{po} r_p / c >> 1$, we obtain $\tilde{B}_\theta(r_p) = 4\pi i \tilde{S}_z(\omega)/(\omega_{po}\omega)$. The inverse transform of this expression leads to the magnetic field given in Eq.(40b)

Figure 2 plots the distribution of the axial Poynting flux, i.e., radiance, $I_z(r,\tau) = cB_\theta^2(r,\tau)/4\pi$ in the (τ, r) plane for $r > r_p$ for laser and plasma parameters $r_p\omega_{po}/c = 25$, $\tau_L\omega_{po}/2\pi = 0.8$, $\omega_o/\omega_{po} = 125$, $\ell = 8$, $\gamma_g \approx 140$, $\lambda_o = 0.8$ μm ($\lambda_p = 100\mu m$), and peak laser intensity $I_{L0} = 7\times10^{13}$ W/cm^2. For these parameters the magnetic field at the surface of the filament is $B_o \approx 9G$. The axial flux is localized in τ to the vicinity of the laser pulse and reaches a maximum of ~18 kW/cm^2 at mid-pulse ($\tau = \tau_L/2$). In the radial direction, the axial flux extends many plasma wavelength beyond the plasma column.

The EMP power propagating in the axial direction resides outside of the plasma filament and is given by

$$P_{EMP}(\tau) = \frac{c}{4\pi}\int_{r_p}^{\infty} B_\theta^2(r,\tau)\,2\pi r\,dr = \frac{c}{16}B_o^2 r_p^2\,\Lambda(\tau,\tau_L), \tag{41}$$

where $\Lambda(\tau,\tau_L) = \ln[(1+\hat{\tau}^2)(1+\Delta\hat{\tau}^2] - 2\,\mathrm{sgn}[\hat{\tau}\Delta\hat{\tau}]\ln[C(\hat{\tau},\hat{\tau}_L)]$,

$$C(\hat{\tau},\hat{\tau}_L) = \frac{2\hat{\tau}^2\Delta\hat{\tau}^2 + \hat{\tau}^2 + \Delta\hat{\tau}^2 + 2|\hat{\tau}||\Delta\hat{\tau}|\left(\hat{\tau}^2\Delta\hat{\tau}^2 + \hat{\tau}^2 + \Delta\hat{\tau}^2 + 1\right)^{1/2}}{\hat{\tau}^2 + \Delta\hat{\tau}^2 + 2|\hat{\tau}||\Delta\hat{\tau}|}, \quad \hat{\tau} = \mathrm{v}_g\gamma_g\tau/r_p,$$

$\hat{\tau}_L = \mathrm{v}_g\gamma_g\tau_L/r_p$ and $\Delta\hat{\tau} = \hat{\tau} - \hat{\tau}_L$. Figure 3 plots $P_{EMP}(\tau)$ normalized to the peak laser power P_L for the same parameters as in Fig. 2. The power ratio is typically very small, with a peak value of $\sim 4\times10^{-10}$. The energy in the EMP pulse is

$$W_{EMP} = \int_{-\infty}^{\infty} d\tau\, P_{EMP}(\tau) = \frac{c}{16}B_o^2 r_p^2 \int_{-\infty}^{\infty} d\tau\,\Lambda(\tau,\tau_L), \tag{42}$$

The energy efficiency, defined as the ratio of the EMP energy to the laser energy, is given by

$$\eta_{Energy} = \frac{W_{EMP}}{W_L} = \frac{\lambda_o^2 I_L}{8\pi P_o}\left(\frac{r_p\omega_{po}}{R_o\omega_o}\right)^2 \Psi(\hat{\tau}_L), \tag{43}$$

where $P_o = m^2c^5/q^2 = 8.75\,\mathrm{GW}$,

$$\Psi(\hat{\tau}_L) \equiv \tau_L^{-1}\int_{-\infty}^{\infty} d\tau\,\Lambda(\tau,\tau_L), \tag{44}$$

and the laser pulse energy is $W_L = (c/16)\left|\hat{E}_L\right|^2 R_o^2 \tau_L$. The function $\Psi(\hat{\tau}_L)$ is plotted in Fig. 4 which shows that it is a slowly increasing function of the variable $\hat{\tau}_L$. The EMP conversion efficiency, Eq.(43), is plotted in Fig. 5. For typical laser parameters the efficiency is extremely small, $\eta_{Energy} \approx 4\times 10^{-10}$.

iii) EMP in the Transient Regime

In this subsection EMP generation for non-steady state, i.e., transient, pulse propagation is discussed. To understand radiative EMP we employ a heuristic model in which the non-steady state regime is represented by a medium varying periodically in the pulse propagation direction. This can represent for example the periodic focusing and defocusing of the laser pulse. Since all the field components can be expressed in terms of the axial electric field we spatially modulate this axial field by the factor $(1 + \varepsilon\cos(\mathrm{K}z))$, where $\mathrm{K} > 0$ is the wavenumber associated with the non-steady state component of the ponderomotive force and ε is a measure of the modulation. In the spatially modulated medium the ponderomotive force has superluminal Fourier components for a range of K. For these values of K the EMP is radiative, resulting in net power flow in the radial direction. This can be understood by noting that the Fourier transform of the axial electric field outside of the filament is given by [see Eq.(23a)],

$$\left(\frac{1}{r}\frac{\partial}{\partial r}\left(r\frac{\partial}{\partial r}\right) - \kappa_{\pm}^2(\omega,K)\right)\tilde{E}_z(\omega,K) = 0, \qquad (45)$$

where

$$\kappa_{\pm}^2(\omega,K) = \kappa_o^2(\omega,\pm K) = \frac{\omega^2}{\mathrm{v}_g^2\gamma_g^2} \pm 2\frac{\omega}{\mathrm{v}_g}\mathrm{K} + \mathrm{K}^2 = \left(\frac{\omega}{\mathrm{v}_g} \pm \mathrm{K}\right)^2 - \frac{\omega^2}{c^2}. \qquad (46)$$

Following Fourier inversion the solutions of Eq.(45) are expressible in the form $K_o(\kappa_{\pm} r)\exp(\pm i\mathrm{K}z)\exp(-i\omega\tau)$. These solutions represent the radial variation of the forward propagating, $\exp(i\mathrm{K}z)$, and the backward propagating, $\exp(-i\mathrm{K}z)$, contributions to the EMP, respectively, where the transverse wavenumber is $\kappa_{\pm}$.

For the purpose of discussing the nature of the solutions, i.e., radiative and non-radiative EMP, we consider the limit of zero collision frequency, $\nu_e = 0$. For $\kappa_{\pm}^2 > 0$ the

solution of Eq. (45) represents exponentially decaying non-radiative solutions, i.e., $K_0(|\kappa_\pm|r) \sim r^{-1/2}\exp(-|\kappa_\pm|r)$. Note that the exponentially increasing solution is non-physical. Since ω and K have been chosen to be positive, κ_+ is always positive and represents exponentially decaying solutions that are non-radiative. However, κ_-^2 can be less than zero for values of K in the range

$$\frac{2\omega}{c} > \mathrm{K} > \frac{\omega}{2c\gamma_g^2}. \tag{47}$$

In this case $\kappa_- = \pm i|\kappa_-|$ and the solution $K_o(\kappa_- r)$ for large r represents radiative solutions, i.e., $K_0(\kappa_- r) \sim r^{-1/2}\exp(\mp i|\kappa_-|r)$. Here, the upper sign represents a radially incoming wave and is not physical. The lower sign, however, represents a radially outgoing EMP field and corresponds to radiative fields. The source of the radiative field is the ponderomotive force containing Fourier components with phase velocities that are superluminal. In the laser pulse frame, the Cherenkov-like emission angle of the EMP radiation with respect to the laser pulse propagation direction is

$$\Theta_c = \tan^{-1}\left(|\kappa_-|/K\right). \tag{48}$$

The phase velocity associated with the Fourier components of the ponderomotive force is given by

$$\mathrm{v}_{ph} = \frac{\omega\,\mathrm{v}_g}{\omega - \mathrm{v}_g\mathrm{K}}, \tag{49}$$

and the EMP is radiative when $\mathrm{v}_{ph} > \mathrm{v}_g$. The radiative and non-radiative branches of the EMP can be illustrated with a dispersion diagram shown in Fig.6. The frequency and wavenumber of the EMP are given by the intersection of the electromagnetic mode and the $\mathrm{v}_{ph} > c$ dispersion line shown in Fig. 6.

III. EMP Generated on the Surface of a Dielectric

In this section we analyze the generation of EMP from dielectric surfaces. The incident laser pulse ionizes the dielectric and produces an oscillating plasma current sheet which is a source of EMP. In addition, we assume that the dielectric may have a non-vanishing second order susceptibility, χ_2; this is the case in crystalline dielectrics. A

second order susceptibility can result in optical rectification and be a source of EMP radiation [43]. Other methods for generating THz radiation in solids are discussed in, for example, [22-25, 44].

In previous sections we found the efficiency of laser energy conversion into EMP energy in air to be extremely small. In this section we consider the EMP generated when a laser pulse is incident on a dielectric target. A difference between a dielectric and the atmosphere is that the electron-neutral collision frequency is nearly-four-orders–of-magnitude larger in dielectrics. Another difference between a dielectric and the atmosphere is related to the ionization process. Typically, to elevate (ionize) an electron from the valence band into the conduction band in a dielectric requires an amount of energy on the order of a few electron volts. Thus for a laser wavelength of $\lambda_o = 0.8\mu m$ $(\hbar\omega_o = 1.54\,\mathrm{eV})$ a few photons suffice to induce photoionization. That is, in Eq.(5), $\ell \approx 2$ and hence the plasma filament is no longer limited to a narrow region near the center of the laser pulse, i.e., the filling factor is nearly unity. Finally, due to the short penetration depth into a dielectric [46], self-focusing and diffraction of the laser beam are negligible and consequently a 1D analysis of the EMP generation suffices. Figure 7 is a schematic illustrating the electromagnetic fields involved in our analysis of EMP generation when an ultrashort laser pulse is incident on a dielectric.

The wave equation for the EMP field inside the dielectric is

$$\nabla\times\nabla\times\mathbf{E} + \frac{n_o^2}{c^2}\frac{\partial^2\mathbf{E}}{\partial t^2} = -\frac{4\pi}{c^2}\frac{\partial\mathbf{J}}{\partial t} - \frac{4\pi}{c^2}\frac{\partial^2\mathbf{P}_2}{\partial t^2}, \tag{50}$$

where n_o is the linear index of the dielectric, the plasma current density, $\mathbf{J}$, is given by Eq.(6), $\mathbf{P}_2 = \chi_2\left|\hat{E}_L\right|^2\hat{\mathbf{e}}_x/2$ is the second order polarization field polarized in the x direction, χ_2 is the second order susceptibility and $\hat{E}_L(z,t)$ is the amplitude of the laser pulse inside the dielectric [41,43]. In writing the second order polarization field, 2nd harmonic terms have been neglected. A typical value for the second order susceptibility in crystalline dielectrics is $\chi_2 \sim 10^{-7}$ esu. On the right hand side of Eq.(50), the ratio of the second order polarization field source term to the radial and axial components of the plasma current density source term, are respectively

$$\left|(\partial \mathbf{P}_2/\partial t)/\mathbf{J}\cdot\hat{\mathbf{e}}_r\right| \sim 4\pi\frac{mc}{q}\frac{\omega_o^2}{\omega_p^2}\frac{\chi_2}{\tau_L}\left(\frac{2\nu_e R_o}{c}\right), \tag{51a}$$

$$\left|(\partial \mathbf{P}_2/\partial t)/\mathbf{J}\cdot\hat{\mathbf{e}}_z\right| \sim 4\pi\frac{mc}{q}\frac{\omega_o^2}{\omega_p^2}\frac{\chi_2}{\tau_L}. \tag{51b}$$

In obtaining Eqs.(51) it was assumed that the process is in the collisionally dominant regime, $\nu_e\tau_L >> 1$. For $\omega_o/\omega_p \sim 10$, $\tau_L \sim 100$ fsec, $\nu_e \sim 10^{15}\,\mathrm{sec}^{-1}$, and spot size of $R_o \sim 200\,\mu$m the ratios in Eqs.(51a,b) are $\sim 10^5$ and 10^2 respectively. This indicates that the optical rectification process, compared to the plasma generation process, can be a far more efficient mechanism for generating EMP in crystalline materials.

To obtain both the current density and second order polarization field on the right hand side of Eq.(50), the laser pulse amplitude $\hat{E}_L$ is required. To obtain the laser pulse amplitude we write the incident, reflected and transmitted laser pulse fields as follows

$$\mathbf{E}_{in}(z,t) = (1/2)E_{in}(t-z/c)\exp[i(k_o z - \omega_o t)]\hat{\mathbf{e}}_x + c.c., \tag{52a}$$

$$\mathbf{E}_R(z,t) = (1/2)E_R(t+z/c)\exp[-i(k_o z + \omega_o t)]\hat{\mathbf{e}}_x + c.c., \tag{52b}$$

$$\mathbf{E}_L(z,t) = (1/2)\hat{E}_L(z,t)\exp(-i\omega_o t)\hat{\mathbf{e}}_x + c.c., \tag{52c}$$

where $k_o = \omega_o/c$ in the vacuum region. The laser field inside the dielectric satisfies

$$\frac{\partial^2 \mathbf{E}_L}{\partial z^2} - \frac{1}{c^2}\frac{\partial^2 \mathbf{E}_L}{\partial t^2} = \frac{4\pi}{c^2}\frac{\partial \mathbf{J}_L}{\partial t} + \frac{4\pi}{c^2}\frac{\partial^2 \mathbf{P}}{\partial t^2}, \tag{53}$$

where $\mathbf{J}_L(z,t)$ and $\mathbf{P}(z,t)$ are respectively, the current density and total polarization fields. Within the dielectric the current density is given by Eq.(2)
where

$$\mathbf{J}_L(z,t) = (1/2)\hat{J}_L(z,t)\exp(-i\omega_o t)\hat{\mathbf{e}}_x + c.c., \tag{54}$$

is the laser driven plasma current density. The rate of change of plasma density is given by Eq.(4a). The polarization field consists of a linear and nonlinear contribution,

$$\mathbf{P}(z,t) = (1/2)\left(P_L(z,t) + P_{NL}(z,t)\right)\exp(-i\omega_o t)\hat{\mathbf{e}}_x + c.c., \tag{55}$$

where $\hat{P}_L(z,t) = \chi_L\hat{E}_L(z,t)$, $\hat{P}_{NL} = \alpha\left|\hat{E}_L(z,t)\right|^2\hat{E}_L(z,t)$, χ_L is the linear susceptibility and α is related to the nonlinear Kerr refractive index. Note that the second order polarization field in Eq.(55) is omitted since it does not contribute to a driving term at the

laser frequency. If the laser pulse duration is long compared to the laser period, i.e., $\omega_o >> |\partial/\partial t|$, Eqs.(53) and (2) can be written as

$$\left(\frac{\partial^2}{\partial z^2} + \frac{\omega_o^2 n_o^2}{c^2}\left(1 + \frac{2i}{\omega_o}\frac{\partial}{\partial t}\right)\right)\hat{E}_L(z,t) = -\frac{4\pi i}{c^2}\omega_o\left(1 + \frac{i}{\omega_o}\frac{\partial}{\partial t}\right)\hat{J}_L(z,t) - \frac{4\pi\omega_o^2}{c^2}\alpha\left|\hat{E}_L\right|^2\hat{E}_L(z,t), \quad (56a)$$

$$\left(1 + \frac{i}{(\omega_o + i\nu_e)}\frac{\partial}{\partial t}\right)\hat{J}_L(z,t) = \frac{i}{4\pi(\omega_o + i\nu_e)}\omega_p^2(z,t)\hat{E}_L(z,t), \quad (56b)$$

where $n_o = (1 + 4\pi\chi_L)^{1/2}$ is the linear refractive index. To lowest order in $\partial/\partial t$, Eqs.(56a) and (56b) combine to give

$$\left(\frac{\partial^2}{\partial z^2} + K^2(z,t) + 2i\frac{\omega_o}{c^2}\left(n_o^2 - \frac{i}{2}\frac{\nu_e}{\omega_o}\frac{\omega_p^2(z,t)}{(\omega_o + i\nu_e)^2}\right)\frac{\partial}{\partial t}\right)\hat{E}_L(z,t) = 0, \quad (57)$$

where

$$K(z,t) = \frac{\omega_o}{c}\left(n_o^2 - \frac{\omega_p^2(z,t)}{\omega_o(\omega_o + i\nu_e)} + 4\pi\alpha\left|\hat{E}_L(z,t)\right|^2 + \frac{\nu_e/\omega_o^2}{(\omega_o + i\nu_e)^2}\frac{\partial\omega_p^2(z,t)}{\partial t}\right)^{1/2}, \quad (58a)$$

$$\frac{\partial\omega_p^2(z,t)}{\partial t} = \frac{2\pi\omega_n^2\omega_o}{(\ell-1)!}\left(\frac{I_L(z,t)}{I_{MP}}\right)^{\ell}. \quad (58b)$$

and $\omega_n^2 = 4\pi q^2 n_{no}/m \sim 1.8\times10^{16}\,\mathrm{sec}^{-1}$ for $n_{no} \sim 10^{23}\,\mathrm{cm}^{-3}$. Note that $4\pi\alpha\left|\hat{E}_L(z,t)\right|^2 = 2n_o n_K (n_n/n_{no}) I_L(z,t)$ where n_K is the nonlinear Kerr refractive index, $n_n = n_{no} - n_e$ and $I_L(z,t) = c n_o \left|\hat{E}_L(z,t)\right|^2/8\pi$ is the laser pulse intensity. For a dielectric the number of photons needed for ionization is typically small, i.e., $\ell = 1$, 2, or 3, for $\lambda_o = 0.8\mu\mathrm{m}$. Equation (57) together with Eqs.(58) describe the evolution of a laser pulse propagating in an ionizing dielectric. In dielectrics collisional and ionization absorption of the laser pulse takes place over a short distance, i.e., the penetration depth is a few microns. For distances short compared to the laser pulse length, i.e., $z << c\tau_L/n_o$, transit time effects can be neglected. In this limit $\partial/\partial t$ can be neglected and Eq.(57) reduces to

$$\left(\frac{\partial^2}{\partial z^2} + K^2(z,t)\right)\hat{E}_L(z,t) = 0. \tag{59}$$

The WKB solution of Eq.(59) is

$$\hat{E}_L(z,t) = \hat{E}_L(0,t)\left(\frac{K(0,t)}{K(z,t)}\right)^{1/2} \exp\left(i\int_0^z dz' K(z',t)\right), \tag{60}$$

where solutions representing waves traveling towards the left are not considered. The value of the field at the boundary, i.e., $\hat{E}_L(0,t)$, is obtained from the boundary conditions. Applying the boundary conditions at $z = 0$, yields

$E_{in}(t) + E_R(t) = \hat{E}_L(0,t)$ and

$E_{in}(t) - E_R(t) = \hat{E}_L(0,t)(K(0,t)+(i/2)(\partial \ln(K)/\partial z)_{z=0})/k_o$ which combine to give

$$\hat{E}_L(0,t) = \frac{2k_o E_{in}(t)}{k_o + K(0,t) + \frac{i}{2}\left(\frac{\partial \ln(K)}{\partial z}\right)_{z=0}}. \tag{61}$$

Within the dielectric the laser pulse amplitude is given by Eq.(60) together with Eq.(62). The laser pulse amplitude determines the current density given by Eq.(2) and the second order polarization field which drives the EMP fields in Eq.(50). These equations are solved numerically in Section IV.

IV. Numerical Simulations of EMP Generation

The numerical simulations presented in this section are based on solving Eq. (20) for the EMP field, with the plasma current and source given by Eqs. (6), (8) and (10). The laser envelope evolves according to Eqs. (14) and the ionization generated plasma density is given by Eq.(15c). The characteristic ionization and recombination parameters used in the simulations are discussed following Eq. (5). The system of equations is solved in axisymetric cylindrical geometry and evolved using a time and space centered finite differencing scheme with the electric field and plasma density calculated on the same grid and the magnetic field and plasma current calculated on a separate, staggered grid. The equations for the EMP fields are solved in the laboratory frame characterized by the variables (r,z,t). The propagation equations for the driving laser pulse are solved

in the group velocity frame and transformed to the laboratory frame when coupled to the EMP equations.

The SDE method [42] of solving for the laser pulse amplitude provides a description of the laser pulse evolution that is simple to implement numerically. However, it is based on the premise that the transverse laser profile is approximately Gaussian. In certain regimes this may be violated as, for example in Fig. 13 of Ref [36], where a hollowing of the laser pulse takes place. In such cases, the solution of Eq. (11) must be employed. In the following we shall assume that the Gaussian profile approximation is valid.

The simulations are initialized at $t = 0$ with the laser pulse propagating in vacuum in the positive z direction. The leading edge of the laser pulse at $t = 0$ is located at axial position $z = 0$. In the vacuum-air transition region from $z = 0$ to $z = L_n$, the neutral density increases with the functional form

$$n_n(z) = n_{no}\begin{cases}1, & z \geq L_n \\ [10(z/L_n)^3 - 15(z/L_n)^4 + 6(z/L_n)^5], & z \leq L_n\end{cases}$$

and has the constant value $n_{no} = 2.7\times10^{19}$ cm^{-3} for $z > L_n$.

a) EMP Generation in Air

The following four examples illustrate the generation of EMP from the interaction of an ultrashort laser pulse with air. The first two examples validate the numerical simulation with the analyses of Sec. III. The third example is a simulation of a recent experiment which observed EMP emitted from a laser pulse propagating in air. The last example in this subsection shows EMP generation from a much higher intensity laser pulse which fully ionizes the air.

i) Steady State Laser Pulse Propagation

This first example benchmarks the numerical simulation with the steady state analysis of Sec. IIIa. A laser pulse propagates through a preformed plasma filament characterized by a constant density $n_e = 10^{17}$ cm^{-3} ($\omega_{po} = 1.9\times10^{13}$ sec^{-1}) in the region $r < r_p$ and $n_e = 0$ for $r > r_p$, where the filament radius is $r_p = 0.4$ mm ($\sim 25\ c/\omega_{po}$). The laser spot size is assumed to be much larger than r_p so that the transverse variation

of the laser envelope can be neglected. To approximate the square laser pulse profile assumed in the analysis, the laser envelope in the simulation is taken to have a longitudinal profile given by $E_L(\tau) = E_{L0} \sin^2[\pi(\tau/\tau_L)^{16}/2]$ for $0 < \tau < \tau_L$ and $E_L(\tau) = 0$, otherwise. The smooth variation of the laser envelope at the leading and trailing edges reduces numerical dispersion. The pulse duration, $\tau_L = 270$ fsec $\sim 0.8 \times 2\pi/\omega_{po}$, is chosen to optimally excite a plasma wave under collisionless conditions. The peak laser intensity is $I_{L0} = 7 \times 10^{13}$ W/cm^2 and the laser wavelength is $\lambda_o = 0.8$ μm. To be consistent with the steady state analysis, the laser envelope is independent of the propagation distance η and the radial EMP source term given by Eq. (10) is neglected in this simulation example.

The length of the vacuum-air transition region for this simulation example is $L_n = 20\, c/\omega_{po} = 0.3$ mm. A transient EMP is generated in this transition region which must be allowed to propagate away from the laser pulse before the steady state is achieved. To achieve steady state, the laser pulse must propagate a distance $z >> 2\gamma_g^2 c\tau_L$. To reduce computer run time and expedite reaching the steady state, a vacuum ($n_o = 1$) is assumed outside of the plasma filament and the laser pulse is given an artificially low group velocity, $\gamma_g = 13$. For these parameters, the minimum propagation distance required to reach steady state is ~ 3 cm.

Figure 8 plots the longitudinal laser intensity profile and axially directed EMP field after a propagation distance of $z = 6.3$ cm. Solid curves denote simulation results and dashed curve denote the results of the steady state analysis given by Eq. (35). Figure 8a compares the laser intensity profile used in the simulation with the theoretical square profile used in the analysis. Figure 8b plots the normalized axial EMP field $\bar{E}_z = |q| E_z / mc\omega_o$ on axis as a function of normalized time $\tau\omega_{po}/2\pi$ and Fig. 8c shows the radial profile of $\bar{E}_z$ at $\tau\omega_{po}/2\pi = 1.4$. The frequency of $\bar{E}_z$ behind the laser pulse is equal to the plasma frequency. There is good agreement between the simulation and the theoretical predictions for both the axial and radial profiles of $\bar{E}_z$. The slight

discrepancy in the EMP field amplitude between the simulation and the analysis apparent in Figs. 8b and 8c is attributable to the difference in pulse shape shown in Fig. 8a.

Figure 9 plots the normalized EMP magnetic field $\overline{B}_\theta = |q| B_\theta / mc\omega_o$ in the steady state corresponding to the simulation of Fig. 8. Figures 9a and 9b plot contours of $\overline{B}_\theta$ in the (τ, r) plane obtained from the steady state analysis and the simulation, respectively. The plots for the steady state analysis were obtained from Eq. (39). Figure 9c shows radial profiles of $\overline{B}_\theta$ taken at mid-pulse ($\tau = \tau_L / 2$) from the simulation (solid curve) and the analysis (dashed curve). There is good agreement between theory and simulation for the amplitude and spatial distribution of $\overline{B}_\theta$ in the steady state regime.

The radial EMP Poynting flux $I_r = c E_z B_\theta / 4\pi$ (solid curve) and laser intensity profile (dashed curve) outside the plasma filament is plotted in Fig. 10a as a function of normalized time $\tau \omega_{po} / 2\pi$. Note the adjacent regions of positive and negative radial flux which, when integrated over time, nearly cancel. This result is consistent with the analytical prediction that the EMP field is non-radiative in the steady state and there is no net radial energy flux. Figure 10b shows that there is, however, a much larger net axial Poynting flux (~ 400 W/cm^2) in the simulation which is in agreement with the analysis. The axial EMP flux is localized longitudinally roughly within the laser pulse.

ii) Transient Laser Pulse Propagation

In the next example, we verify the condition for radiative EMP given by Eq. (47). A laser pulse with longitudinal profile given by $E_L(\tau) = E_{L0} \sin[\pi\tau / 2\tau_L]$ for $0 < \tau < \tau_L$ and $E_L(\tau) = 0$, otherwise, pulse duration $\tau_L = 270$ fsec $\sim 0.8 \times 2\pi / \omega_{po}$, peak laser intensity $I_{L0} = 7 \times 10^{13}$ W/cm^2, and wavelength $\lambda_o = 0.8$ μm propagates through a modulated, preformed plasma filament. The plasma density is given by $n_e(r,z) = n_{eo}[1 - \Theta(r - r_p)][1 + \varepsilon \sin(Kz)]$, where $n_{eo} = 10^{17}$ cm^{-3}, the modulation amplitude is $\varepsilon = 0.3$ and $\Theta(x)$ is the Heaviside unit step function. As in the previous example, there is a transition region from vacuum to air with a scale length $L_n = 20\, c / \omega_{po} = 0.3$ mm. The linear and nonlinear (Kerr) indicies of air are chosen to be $n_o - 1 = 2.7 \times 10^{-4}$ and $n_K = 6 \times 10^{-19}$ cm^2/W, respectively. For these parameters, the

relativistic factor associated with the laser group velocity [see Eq. (22)] has the value $\gamma_g = 109$. The laser envelope is taken to be independent of the propagation distance η and the radial EMP source term given by Eq. (10) is neglected to be consistent with the analysis. Note that for an unmodulated plasma filament, the distance required to reach steady state for these parameters is $\sim 2\,\mathrm{m}$.

Figures 11 and 12 compare the spatial EMP distribution generated from two plasma filaments modulated with different wavelengths. In Fig. 11, the modulation wavenumber, $K = \omega_{po}/4c$, is chosen to satisfy the condition for radiative EMP given by Eq. (47) assuming that the characteristic frequency $\omega \sim \omega_{po}$. Figure 11a plots the spatial $(\xi = z - \mathrm{v}_g t,\ r)$ distribution of the radial Poynting flux, I_r, after a propagation distance of $\sim 2\,\mathrm{cm}$. Radiative EMP is observed propagating from the plasma channel behind the laser pulse. The radiation is confined to a cone characterized by the Cherenkov angle given by Eq. (48). The outward EMP flux observed within the laser pulse $(-80\,\mu\mathrm{m} < \xi < 0)$ is a manifestation of the transient interaction at the vacuum-air transition region. It is expected that there would be no net outward flux in the region $-80\,\mu\mathrm{m} < \xi < 0$, had the simulation reached the steady state regime after 2 m of propagation. In Fig. 11b, the radial profile of I_r behind the laser pulse at axial position $\xi = -220\ \mu\mathrm{m}$ shows an outward Poynting flux on the order of 100 W/cm^2 extending outside the plasma filament.

In Fig. 12, simulation parameters are identical to those of Fig. 11, except that the modulation wavenumber, $K = 4\omega_{po}/c$, is chosen to be larger than the maximum value for radiative EMP, assuming $\omega \sim \omega_{po}$. Consistent with the analysis, Fig. 12a shows an absence of radial flux behind the laser pulse outside the plasma filament. Behind the laser pulse, the EMP is confined within the plasma filament. The radial profile of I_r in Fig. 12b shows that while there is a larger radial EMP flux within the plasma filament relative to the simulation of Fig. 11, it is highly evanescent outside of the plasma filament. Again, the outward flux observed in the region $-80\,\mu\mathrm{m} < \xi < 0$ is due to the transient interaction at the vacuum-air transition region, and is not present in the steady state regime.

iii) Comparison with Experiment

A recent experiment reported in Ref. [17], measured an EMP from a femtosecond laser pulse propagating in air. In the experiment, a laser pulse with a FWHM duration of 120 fsec, wavelength $\lambda_o = 0.8$ μm, and energy ~30 mJ was passed through an aperture of diameter 1.5 cm and focused into the air with a 2 m focal length lens. As the laser pulse focused and the intensity increased, a plasma filament was formed near the focal region and EMP was measured along the length of the plasma filament. The following results are from a simulation with similar parameters.

In our simulation, the parameters for air are taken to be $n_o - 1 = 2.7\times10^{-4}$, $n_K = 3\times10^{-19}$ cm^2/W, $U_{ion} = 12$ eV, $\ell = 8$, $I_{MP} = 10^{14}$ W/cm^2, and $n_{no} = 2.7\times10^{19}$ cm^{-3}. The laser pulse envelope is taken to be Gaussian in the transverse direction with a spot size $R_o = 7.5$ mm. The longitudinal laser field profile is given by Eq. (25) with $\tau_L = 240$ fsec, which corresponds to a FWHM intensity duration of 120 fsec. The laser pulse has wavelength $\lambda_o = 0.8$ μm, peak power $P_L = 83$ GW and energy ~ 10 mJ. The simulation is performed in two parts as illustrated in Fig. 13. The first part models the focusing of the initially low intensity laser pulse in air by a lens with a focal length of 2 m. Here the simulation covers a range $0 < z < z_o$, where $z_o = 1.82$ m. Over this range, the laser intensity is sufficiently low that no appreciable plasma density is formed and no EMP is generated. To expedite the simulation, only the propagation equations for the driving laser pulse envelope are solved for $z < z_o$. The laser pulse envelope at $z = z_o$ is used to initialize the full-scale EMP simulation for $z > z_o$.

Figure 14a plots the peak plasma density (solid curve) and laser intensity (dashed curve) over the range $0 < \Delta z < 16$ cm, where $\Delta z = z - z_o$ is the distance from the start of the full-scale EMP simulation. For $\Delta z < 9$ cm, the laser intensity increases due to both geometric and nonlinear focusing. For $\Delta z > 9$ cm, a plasma filament is formed on axis which defocuses the trailing edge of the laser pulse, thereby resulting in a shorter duration laser pulse. The peak plasma density achieved in the simulation is $\sim 2\times10^{18}$ cm^{-3}, which occurs at $\Delta z \sim 10$ cm. For $\Delta z > 10$ cm the plasma density

steadily decreases due to the shortening of the laser pulse. Figure 14b plots the corresponding peak values of the axial (solid curve) and radial (dashed curve) Poynting fluxes as a function of Δz. The maximum EMP flux coincides with the maximum plasma density. The maximum radial flux is $I_r \sim 35$ kW/cm^2 while the maximum axial flux is $I_z \sim 15$ kW/cm^2. Significant shortening of the driving laser pulse prevented the simulation from extending beyond $\Delta z \sim 16$ cm without violating the assumption that group velocity dispersion is negligible.

Figure 15 plots the spatial distribution of the laser intensity and the various EMP field components at $\Delta z \sim 10$ cm, when the plasma density is maximum. The plasma filament radius in these plots is $r_p \sim 100\,\mu m$. The hour-glass shaped laser intensity contours show nonlinear Kerr self-focusing, i.e., the higher intensity middle region of the pulse has a smaller spot size than the lower intensity leading and trailing edges. In addition, plasma defocusing is evident from the slightly larger spot size in the trailing regions of the pulse where the plasma density is higher. The axial EMP electric field is localized within the plasma filament while the magnetic field and radial electric field extend beyond the transverse dimension of the filament.

Figures 16a and 16b plot the spatial distribution of the radial and axial Poynting flux at $\Delta z \sim 10$ cm, respectively. Inside the plasma filament, the Poynting fluxes are peaked within the laser pulse and decay in amplitude behind the pulse. The radial flux is mainly confined within the plasma filament while the axial flux extends radially beyond the filament. Although not apparent from the color scale of the plot, a small radial flux is present outside of the filament which can be experimentally detected. Figure 17a plots the on axis laser intensity (normalized to its peak value at $z = 0$) versus time at $\Delta z = 10$ cm (dashed curve) and $\Delta z = 12$ cm (solid curve). The relatively shorter pulse duration at $\Delta z = 12$ cm is the result of plasma defocusing of the trailing edge of the laser. Figure 17b plots the corresponding radial Poynting flux versus time at radial position $r = 225$ μm. The Poynting flux is peaked in a region behind the driving laser pulse and has a duration that is of the order $\sim 1/\nu_e$. Note that the flux at $\Delta z = 10$ cm is directed radially outward while at $\Delta z = 12$ cm, it is outward just behind the laser pulse and then

reverses direction. Figure 17c plots the frequency distribution of the two curves shown in Fig. 17b. The frequency distribution

$$\psi_r(r_0,\omega) \equiv \frac{\Delta\omega}{\sqrt{2\pi}} \int_{-\infty}^{\infty} I_r(r_0,t) e^{i\omega t}\, dt, \tag{63}$$

has units of intensity and represents the intensity contained within a frequency band $\Delta\omega$, which, for a laboratory experiment, is typically the resolution of the detector used to measure the EMP. In this case, $\Delta\omega/2\pi \sim 1$ THz is the smallest frequency interval that can be resolved by the simulation grid size. The EMP spectrum at $\Delta z = 10$ cm is peaked near zero frequency and is broadband with a width of ~10 THz. At $\Delta z = 10$ cm, the maximum electron collision frequency $\nu_e \sim 6\times10^{13}$ sec^{-1}. At $\Delta z = 12$ cm, the spectrum is broader and a local maximum at a frequency of ~ 2 THz is apparent. The peak plasma frequency varies from ~ 13 THz to ~ 12 THz over the 2 cm of propagation shown in the plots. Note that there is no distinct feature in the EMP spectrum at the plasma frequency or any of its harmonics.

Figure 18 plots the total EMP power emitted radially through a cylindrical surface of radius $r_o = 580$ μm versus time, i.e.,

$$P_r(t) = 2\pi r_o \int_{-\infty}^{\infty} I_r(r_o,z,t)\, dz\,. \tag{64}$$

Note that time $t = 0$ in the plot corresponds to the instant the laser pulse reaches the axial position $z = z_0$. The power has a maximum of ~ 0.8 W. Most of the power is emitted over a duration ~ 0.1 nsec. Integrating the curve in Fig. 18 over time, the total energy radiated in the radial direction during the entire simulation is found to be ~ 50 pJ.

iv) High Energy Laser Pulse

As a final example of atmospheric EMP generation, we consider the propagation of a high-energy (~ 1 J), high-intensity ($> 10^{14}$ W/cm^2) ultrashort laser pulse in air. In this example, the initial laser pulse is Gaussian in the transverse direction with a spot size $R_o = 1$ mm. The longitudinal envelope is given by

$$|E_L(0,z,\tau)| = \hat{E}_L(z)\sin^2(\pi\tau/\tau_L) \tag{65}$$

for $0 \le \tau \le \tau_L$ and zero otherwise, with $\tau_L = 240$ fsec. The laser pulse is initially collimated and has wavelength $\lambda_o = 0.8$ μm, peak power $P_L = 5.3$ TW, intensity $I_{L0} = 3.5\times10^{14}$ W/cm^2, and energy ~ 0.5 J. Parameters for air are taken to be $n_o - 1 = 2.7\times10^{-4}$, $n_K = 3\times10^{-19}$ cm^2/W, $U_{ion} = 12$ eV, $\ell = 8$, and $I_{MP} = 10^{14}$ W/cm^2. The air-vacuum interface has scale length ~ 70 μm.

Figure 19a shows the normalized peak laser intensity, I_L / I_{L0} and normalized peak plasma density n_e / n_{no} as a function of propagation distance. At $z = 0$, the laser pulse is in vacuum. As the laser pulse enters the air, the air is fully ionized and the laser intensity decreases rapidly. Note that for the initial parameters of the simulation, the scale length for laser energy depletion due to ionization is $\sim 8\ \mu m$. Over a propagation distance of ~ 1 cm, the laser pulse is seen to lose more than ~ 70% of its energy. As the laser intensity decreases, the plasma density is also seen to decrease. The corresponding values of peak radial and axial Poynting flux are plotted in Fig. 19b. Initially, the peak radial flux (~ 1 MW/cm^2) is much larger than the peak axial flux (~ 26 kW/cm^2). After ~ 1 cm of propagation, the radial and axial flux are both of order ~ 1 kW/cm^2. Note that a quasi-equilibrium state is attained after ~0.3 cm of propagation in which the laser intensity and plasma density change slowly relative to the initial phase of propagation in which the air was close to fully ionized.

Figure 20 plots the corresponding spatial distributions of laser intensity, and Poynting flux in the quasi-equilibrium configuration at a propagation distance $z = 0.8$ cm. The radius of the plasma filament is these plots is ~ 0.5 mm. Due to the high electron collision frequency, there is little axial flux in the region $r < 0.25$ mm, while the radial flux is seen to be strongly damped behind the laser pulse.

b) EMP Generation on the Surface of a Dielectric

In this subsection, we simulate the EMP generation from the interaction of a laser pulse with a dielectric surface. The simulation is set up with air in the region $z < 0$, and a dielectric in the region $z > 0$, as indicated in Fig. 7. The initial laser pulse at $t = 0$ is situated just outside the dielectric and has a field envelope that is Gaussian in the

transverse direction with a spot size $R_o = 0.1$ mm. The longitudinal laser field profile is given by Eq.(25) with $\tau_L = 200$ fsec. The laser pulse has wavelength $\lambda_o = 0.8$ μm ($\hbar\omega_o = 1.54$ eV), and peak intensity $I_L = 10^{13}$ W/cm^2. The dielectric is characterized by $n_{no} = 6\times10^{22}$ cm^{-3}, $n_o = 3$, $n_K = 7\times10^{-15}$ cm^2/W, $U_{ion} = 3$ eV, $\ell = 2$, and $I_{MP} = 5\times10^{14}$ W/cm^2. The WKB solution, i.e., Eq. (60), is evaluated numerically to obtain evolution of the laser pulse within the dielectric, and Eq.(50) is solved to determine the EMP generation.

Figure 21 plots contours of the laser intensity, I_L, and EMP intensity, $I_{EMP} = (I_r^2 + I_z^2)^{1/2}$ in the (z,r) plane at various times during the simulation. Fig 21a shows the laser intensity contours before the interaction at $t = 0$. Figure 21b shows the simulation results immediately after the front of the laser pulse enters the dielectric and the initial EMP is generated. The EMP extends radially on the order of the laser spot size and longitudinally ~ 50 μm into the dielectric. The EMP has a peak intensity of $I_{EMP} \sim 30$ MW/cm^2 near the boundary. At this time, a plasma layer of width ~5μm, radial extent ~ 100 μm, and peak density $n_e \sim 3.5\times10^{21}$ cm^{-3} ($\omega_p \sim 3.3\times10^{15}$ sec^{-1}) is formed at the boundary. The laser pulse is absorbed within several microns of the boundary.

Figure 21c shows the EMP as the trailing end of the laser pulse approaches the boundary. At this instant, the peak EMP intensity is $I_{EMP} \sim 7$ MW/cm^2 within the dielectric. Outside the dielectric, an EMP traveling in the negative z direction is observed. Figure 21d shows simulation results later in time after the laser pulse has been completely absorbed in the dielectric. There is relatively little EMP flux within the dielectric; most of it has been either reflected or absorbed by the plasma. At this time, the peak plasma density is $n_e \sim 9\times10^{21}$ cm^{-3}. Within the dielectric, a pulse of intensity ~ 300 kW/cm^2 traveling in the positive z direction is observed.

V. Summary

In this paper the generation of EMP by ultrashort laser pulses in air and on dielectric surfaces is analyzed and discussed. Multi-photon ionization leads to the creation of a plasma filament in the medium. The plasma currents driven by the ponderomotive forces associated with the laser pulse are the source of the EMP. The plasma currents, however, decay rapidly behind the laser pulse due to the large electron collision frequency. For a plasma density of $n_e \sim 10^{16}\,\mathrm{cm}^{-3}$, the electron collision frequency is $\nu_e \sim 5\times10^{12}\,\mathrm{sec}^{-1}$ (for $T_e = 1\,\mathrm{eV}$) and the duration of the plasma current is $\sim 1/\nu_e \sim 200\,\mathrm{fsec}$. The duration of the EMP at a fixed axial position is roughly equal to the laser pulse duration plus the plasma decay time, $\sim \tau_L + 1/\nu_e$, which is typically a few hundred femtoseconds. The conversion efficiency from the laser pulse to EMP radiation is found to be extremely small in both air and on dielectric surfaces. Typical conversion efficiencies are on the order of 10^{-9}. The EMP frequency spectrum is broad with a characteristic frequency determined by the laser pulse duration and the electron collision time and not by the local plasma frequency. Our results are fundamentally different from those in [30, 31]. For example, in a steady-state propagation regime the EMP is non-radiative and the energy flux is axially directed with no net radial component. We show that in a transient propagation regime radiative flux of EMP energy is possible provided a Cherenkov-like condition is satisfied. Several examples of EMP generation have been simulated and discussed. Our results predict a peak EMP power of ~ 0.8 W for the parameters of the experiment in Ref. 17, corresponding to an efficiency of $\sim 10^{-9}$ for the radial power flow. In another example, using a high energy laser pulse (0.5 J) we find that the ionization losses of the laser pulse are significant and that the pulse eventually reaches a quasi-equilibrium state. Finally, simulations of EMP generation from the interaction of a laser pulse with a dielectric medium show that EMP intensities on the order of a $\mathrm{MW/cm}^2$ can be generated. Most of the EMP energy, however, is reflected by the plasma formed at the surface of the dielectric.

Acknowledgement

The authors thank Drs. Antonio Ting, and Daniel Gordon, Vern Schlie and Arie Zigler for useful discussions. This work was sponsored by the Office of Naval Research,

References

[1] A. Braun, G. Korn, X. Liu, D. Du, J. Squier, and G. Mourou, Opt. Lett. **20**, 73 (1995).

[2] E.T. Nibbering, P.F. Curley, G. Grillon, B.S. Prade, M.A. Franco, F. Salin, and A. Mysyrowicz, Opt. Lett. **21**, 1 (1996).

[3] O.G. Kosareva, V.P. Kandidov, A. Brodeur, C.Y. Chien, and S.L. Chin, Opt. Lett. **22**, 1332 (1997).

[4] L. Woste, C. Wedekind, H. Wille, P. Rairoux, B. Stein, S. Nikolov, Ch. Werner, St. Niedermeier, F. Ronneberger, H. Schillinger, and R. Sauerbrey, Laser Optoelektron **29**, 51 (1997).

[5] B. La Fontaine, F. Vidal, Z. Jiang, C.Y. Chien, D. Comtois, A. Desparois, T.W. Johnston, J.-C. Kieffer, H. Pepin, and H.P. Mercure, Phys. Plasmas **6**, 1615 (1999).

[6] S. Tzortzakis, L. Berge, A Couairon, M. Franco, B. Prade, and A. Mysyrowicz, Phys. Rev. Lett. **86**, 5470 (2001); A. Couairon, S. Tzortzakis, L. Berge, M. Franco, B. Prade, and A. Mysyrowicz, J. Opt. Soc. Am. B 19, 1117 (2002).

[7] C.Y. Chien, B. La Fontaine, A Desparois, Z. Jiang, T.W. Johnston, J.-C. Kieffer, H. Pepin, F. Vidal, and H.P. Mercure, Opt. Lett. **25**, 578 (2000).

[8] J. Kasparian, R. Sauerbrey, D. Mondelain, S. Niedermeier, J. Yu, J.-P. Wolf, Y.-B. Andre, M. Franco, B. Prade, S. Tzortzakis, A. Mysyrowicz, M. Rodriguez, H. Wille, and L. Woste, Opt. Lett. **25**, 1397 (2000).

[9] J. Yu, D. Mondelain, G. Ange, R. Volk, S .Niedermeier, J.P. Wolf, J. Kasparian, and R. Sauerbrey, Opt. Lett. 26, 533 (2001).

[10] X. M. Zhao, J.-C. Diels, C.Y. Wang, and J.M. Elizondo, IEEE J. Quant. Elec. **31**, 599 (1995).

[11] H. Schillinger and R. Sauerbrey, Appl. Phys. B **68**, 753 (1999).

[12] S. Tzortzakis, M.A. Franco, Y.-B. Andre, A. Chiron, B. Lamouroux, B.S. Prade, and A. Mysyrowicz, Phys. Rev. E 60, R3505 (1999).

[13] D. Comtois, C.Y. Chien, A Desparois, F. Genin, G. Jarry, T.W. Johnston, J.-C. Kieffer, B. La Fontaine, F. Martin, R. Mawassi, H. Pepin, F.A.M. Rizk, F. Vidal, P. Couture, H.P. Mercure, C. Potvin, A. Bondiou-Clergerie, and I. Gallimberti, Appl. Phys. Lett. **76**, 819 (2000).

[14] H.D. Ladouceur, A.P. Baronavski, D. Lohrmann, P.W. Grounds, and P.G. Girardi, Opt. Commun. **189**, 107 (2001).

[15] A. Ting, D. Gordon, D. Kaganovich, E. Briscoe, C. Manka, J. Peñano, P. Sprangle, B. Hafizi, and R. Hubbard, "Experiments on the Propagation and Filamentation of Ultrashort Intense Laser Pulses in Air", to be published in Journal of Directed Energy (2003).

[16] Proulx, A. Talebpour, S. Petit and S.L. Chin, Opt. Commun. **174**, 305 (2000).

[17] S. Tzortzakis, G. Méchain, G. Patalano, Y.B. André, B. Prade, M. Franco, A. Mysyrowicz, J.M. Munier, M. Gheudin, G. Beaudin and P. Encrenaz, Opt. Lett. **27**, 1944 (2002).

[18] J. Kasparian, M. Rodriguez, G. Mejean, J. Yu, E. Salmon, H. Wille, R. Bourayou, S. Frey, Y.-B. Andre, A. Mysyrowicz, R. Sauerbrey, J.-P. Wolfe, L. Woste, Science **301**, 61 (2003).

[19]. G. Kozlov and A. Volkov, Chapter 3, page 52 in **Millimeter and Submillimeter Wave spectroscopy of Solids**, Edited by G. Grüner, Springer-Verlag (Berlin, Heidelberg, New York) 1998

[20]. T. Idehara et al., IEEE Trans. On Nucl. Science 27,340 (1999)

[21]. G. L. Carr et al., Phys. Med. Biol. 47, 1 (2002)

[22]. Z. Jiang and X. C. Zhang, page 155 in **Sensing with Terahertz Radiation,** Edited by D. Mittleman, Springer-Verlag (Berlin, Heidelberg, New York) 2003

[23]. M. C. Nuss and J. Orenstein, Chapter 2, page 7 in **Millimeter and Submillimeter Wave spectroscopy of Solids**, Edited by G. Grüner, Springer-Verlag (Berlin, Heidelberg, New York) 1998

[24]. K. Kawase et al., Riken Review 47, 48 (2002)

[25]. E. Bründermann, D. R. Chamberlin and E. E. Haller, Appl. Phys. Lett. 76 2991 (2000)

[26]. E. R. Mueller, Submillimeter Wave Lasers, page 597 in **Encyclopedia of Electrical and Electronic Engineering,** Vol. 20, Edited by J. G. Webster, John Wiley &Sons, Inc (New York) 1999

[27]. C. H. Lai et al., Phys. Rev. Lett. 77, 4764 (1996); D. Hashimshony et al., Phys. Rev. Lett. 86, 2806 (2001)

[28]. N. Yugami et al., Phys. Rev. Lett. 89, 5 Aug. (2002)

[29] P. Sprangle, E. Esarey, A. Ting and G. Joyce, Appl. Phys. Lett. 53, 2146 (1988); P. Sprangle, B. Hafizi, J.R. Peñano, R.F. Hubbard, A. Ting, A. Zigler and T.M. Antonsen, Phys. Rev. Lett. 85, 5110 (2000); P. Sprangle, B. Hafizi, J.R. Peñano, R.F. Hubbard, A. Ting, C.I. Moore, D.F. Gordon, A. Zigler, D. Kaganovich and T.M. Antonsen, Phys. Rev. E 63, 056405 (2001).

[30] C.C. Cheng, E.M. Wright and J.V. Moloney, Phys. Rev. Lett. 87, 213001 (2001).

[31] C.C. Cheng, E.M. Wright and J.V. Moloney, Phys. Rev. Lett. 89, 139302 (2002).

[32] G. Shvets, I. Kaganovich and E. Startsev, Phys. Rev. Lett. 89, 139301 (2002).

[33] J.R. Peñano, P. Sprangle, P. Serafim, B. Hafizi and A. Ting, "Stimulated Raman Scattering of Intense Laser Pulses in Air," submitted to Phys. Rev. E, (2003), also "Stimulated Raman Scattering of Intense Free-Electron Laser Radiation in the Atmosphere", to be published in Journal of Directed Energy (2003).

[34] P. Sprangle, E. Esarey, and B. Hafizi, Phys. Rev. Lett. 79, 1046 (1997); P. Sprangle, E. Esarey, and B. Hafizi, Phys. Rev. E 56, 5894 (1997); P. Sprangle, B. Hafizi and J.R. Peñano, Phys. Rev. E 61, 4381 (2000).

[35] ***NRL Plasma Formulary***, edited by J. D. Huba, Naval Research Laboratory Publication NRL/PU/6790-98-358 (U.S. GPO, Washington, D.C., 1998).

[36] P. Sprangle, J.R. Peñano and B. Hafizi, Phys. Rev. E 66, 046418 (2002).

[37] L.V. Keldysh, Zh. Eksp. Teor. Fiz. **47**, 1945 (1964) [Sov. Phys. JETP **20**, 1307 (1965)]

[38] B. La Fontaine, F. Vidal, Jiang, C.Y. Chien, D. Comtois, A. Desparois, T.W. Johnston, J.–C. Kieffer, H. Pepin, and H. P. Mercure, Phys. Plasma **6**, 1615 (1999).

[39] A.W. Ali, "On electron beam ionization of air and chemical reactions for distrurbed air deionization", Naval Research Laboratory Memorandum Report 4619 (1981).

[40] P. Sprangle, J. R. Peñano, A. Ting, B. Hafizi and D. F. Gordon, "Propagation of Short High Intensity Laser Pulses in Air", to be published in Journal of Directed Energy (2003).

[41] R.W. Boyd, *Nonlinear Optics* (Academic, San Diego, (1992).

[42] P. Sprangle, A. Ting and C. M. Tang, Phys. Rev. A 36, 2773 (1987).

[43] D.H. Auston, Applied Physics Letters, **43**, 713 (1983).

[44] S.C. Howells and L.A. Schlie, Appl. Phys. Lett. **67**, 3688 (1995).

[45] H.M. Milchberg and R.R. Freeman, J. Opt. Soc. Am. B, **6**, 1351 (1989).

[46] C.H. Lee, *Picosecond Optoelectronic Devices* (Academic, Orlando, 1984)

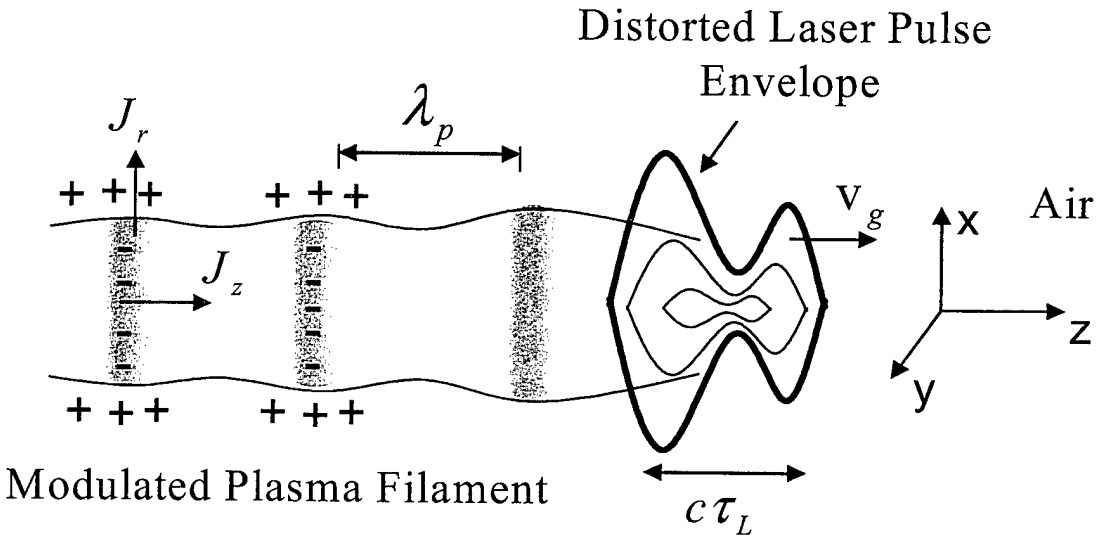


Figure 1. Schematic diagram for atmospheric EMP generation. A ultra-short laser pulse ionizes the air and forms a plasma filament. The ponderomotive forces associated with the laser pulse envelope drive radial and axial currents, J_r and J_z, respectively, which are the source of EMP. The laser pulse distorts due to ionization and the optical Kerr effect. The filament is modulated at the plasma wavelength, λ_p. The axial EMP electric field outside the filament is small due to shielding by surface charges at the air-plasma boundary.

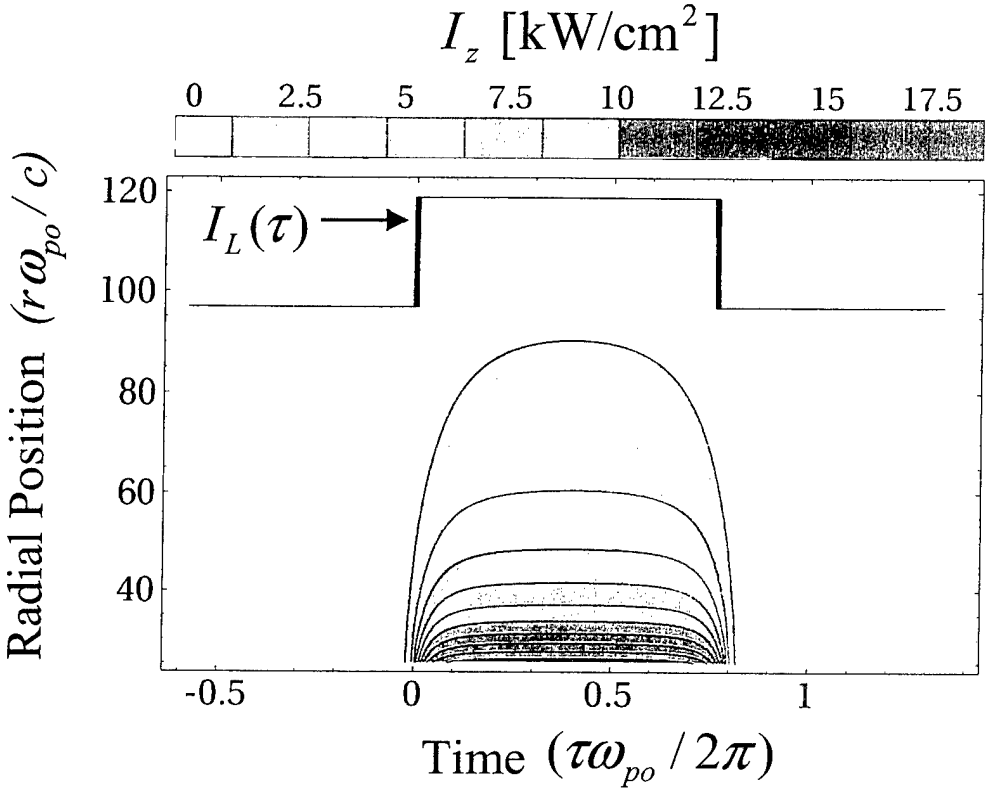


Figure 2: (a) Distribution of axial Poynting flux ($I_z = cB_\theta^2/4\pi$) outside the plasma channel in the (τ, r) plane for steady state propagation where B_θ is obtained from Eq. (39). Shaded contours are obtained for the parameters $n_{eo} = 1.1\times10^{17}$ cm^{-3}, $r_p = 0.4$ mm $(= 25\, c/\omega_{po})$, $\tau_L = 267$ fsec, $\lambda_o = 0.8$ μm $(\omega_o/\omega_{po} = 125)$, $\gamma_g \approx 109$, and $I_{L0} = 7\times10^{13}$ W/cm^2. Laser intensity profile, $I_L(\tau)$, indicates that in the steady state, the EMP duration is comparable with the laser pulse duration.

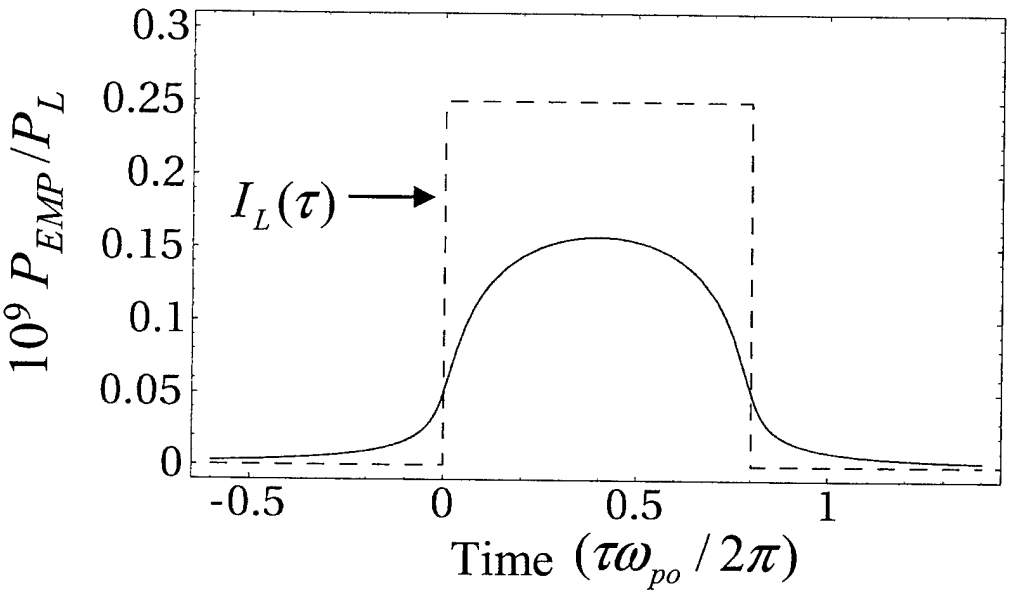


Figure 3: Axially propagating EMP power (solid curve), i.e., $P_{EMP}(\tau)$ from Eq. (41), normalized to the peak laser power P_L = 2.8 TW for steady state propagation. Dashed curve indicates longitudinal laser intensity profile $I_L(\tau)$. Parameters are identical to those of Fig 2. In calculating P_L, it is assumed that the laser spot size is $R_o = r_p\sqrt{2\ell}$, where $\ell = 8$ is the multiphoton ionization order of Eq. (5).

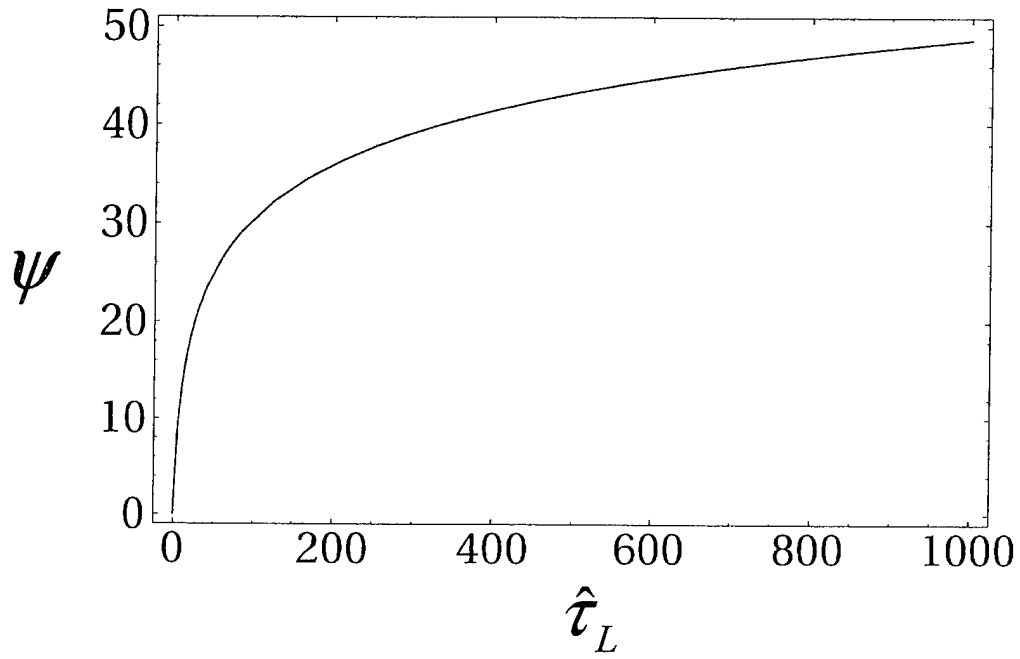


Figure 4: The function $\psi(\hat{\tau}_L)$ of Eq. (44) as a function of normalized pulse duration $\hat{\tau}_L$.

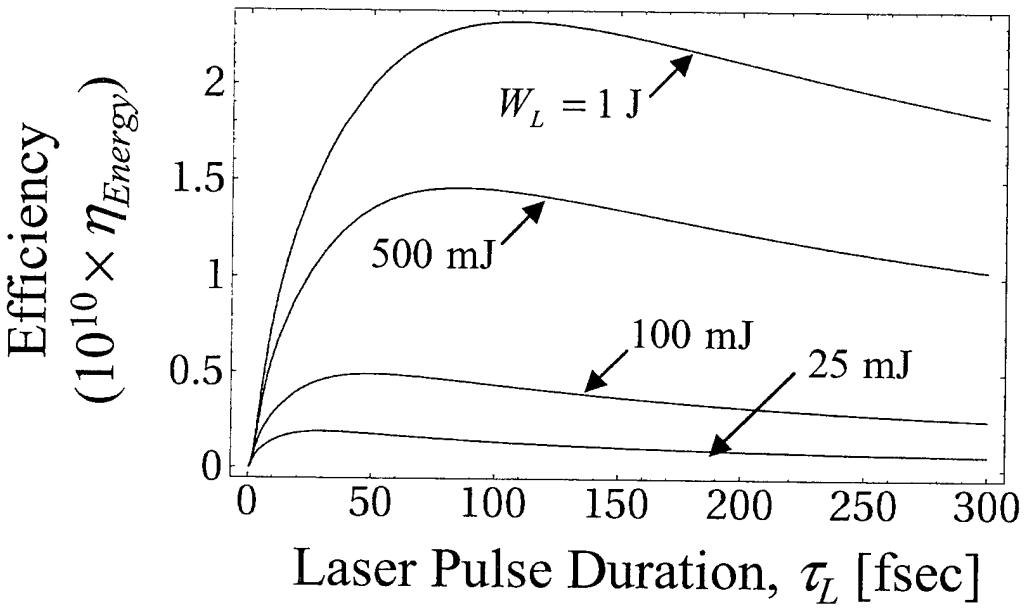


Figure 5: Steady state EMP conversion efficiency given by Eq. (43) vs. laser pulse duration for various laser pulse energies.

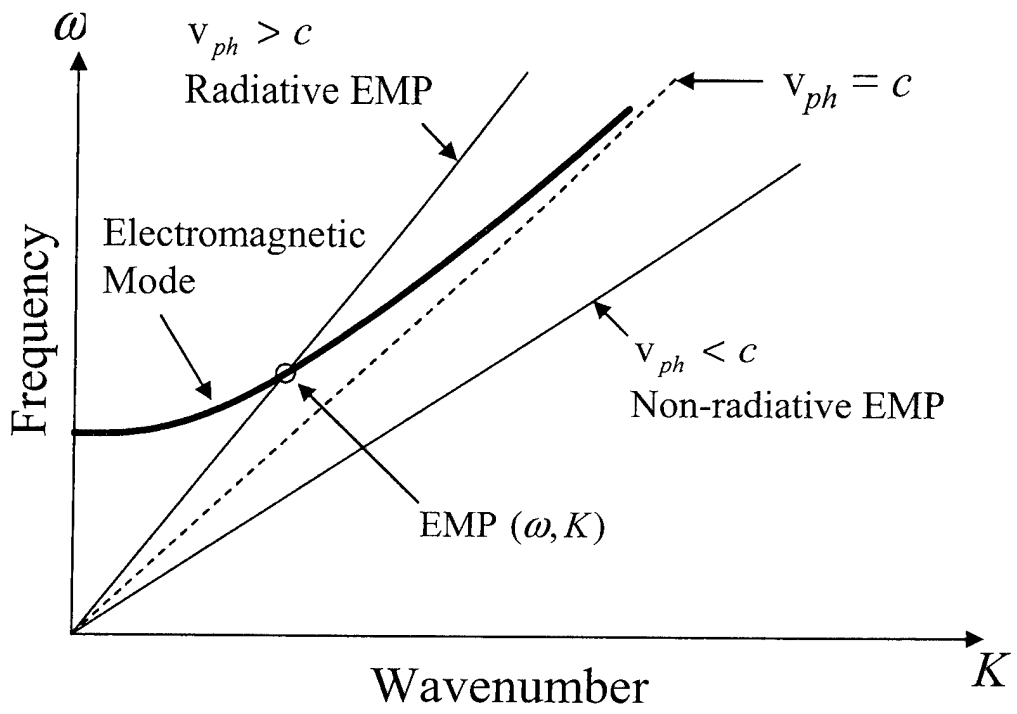


Figure 6: Dispersion diagram showing the condition for radiative EMP.

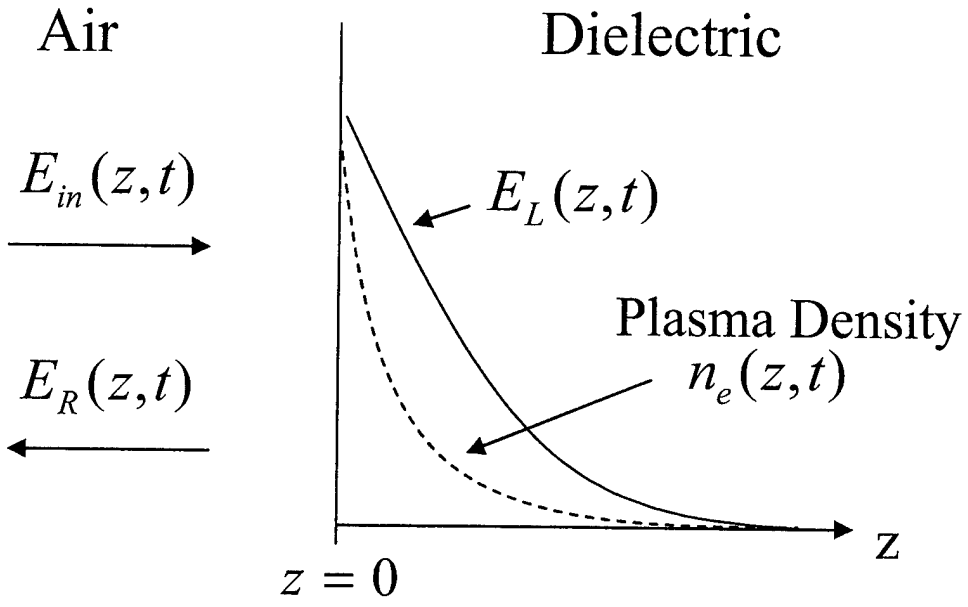


Figure 7: Schematic diagram of intense laser beam incident on a dielectric surface.

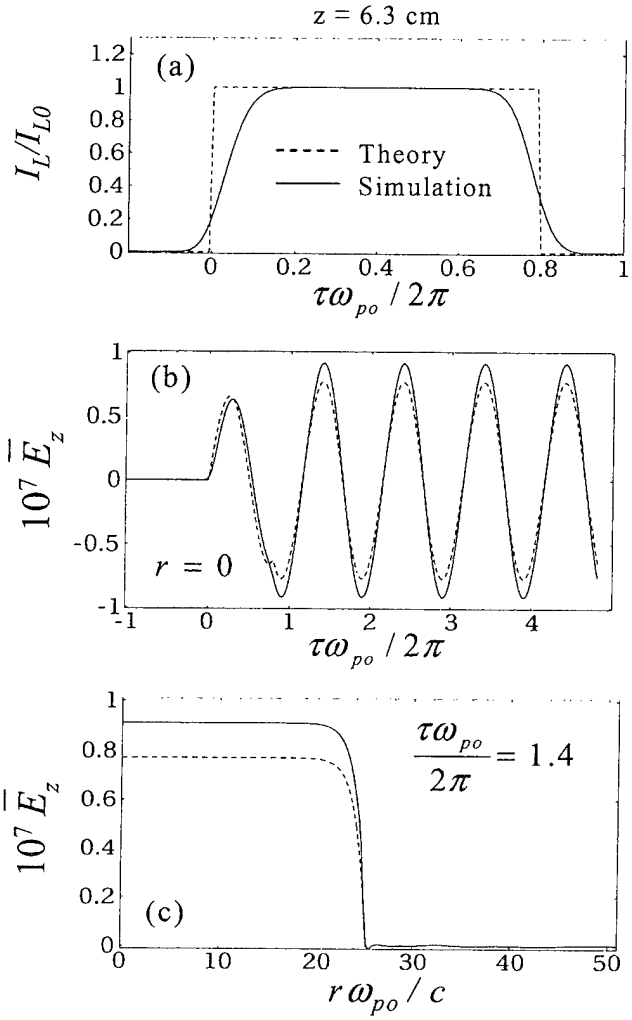


Figure 8: Comparison of longitudinal electric field E_z obtained from numerical simulation (solid curves) and steady state analysis (dashed curves). Plots show (a) normalized laser intensity vs. τ, (b) normalized electric field, $\bar{E}_z = |q|E_z/mc\omega_0$, vs. τ at $r = 0$, and (c) $\bar{E}_z$ vs. radial position at $\tau\omega_{po}/2\pi = 1.4$. Laser parameters are $\lambda_o = 0.8$ μm, $\tau_L = 267$ fsec, $\gamma_g = 13$, and peak laser intensity $I_{L0} = 7\times10^{13}$ W/cm^2. Plasma parameters are $n_{eo} = 1.1\times10^{17}$ cm^{-3} and $r_p = 0.4$ mm. Simulation results are plotted at a propagation distance of $z = 6.3$ cm.

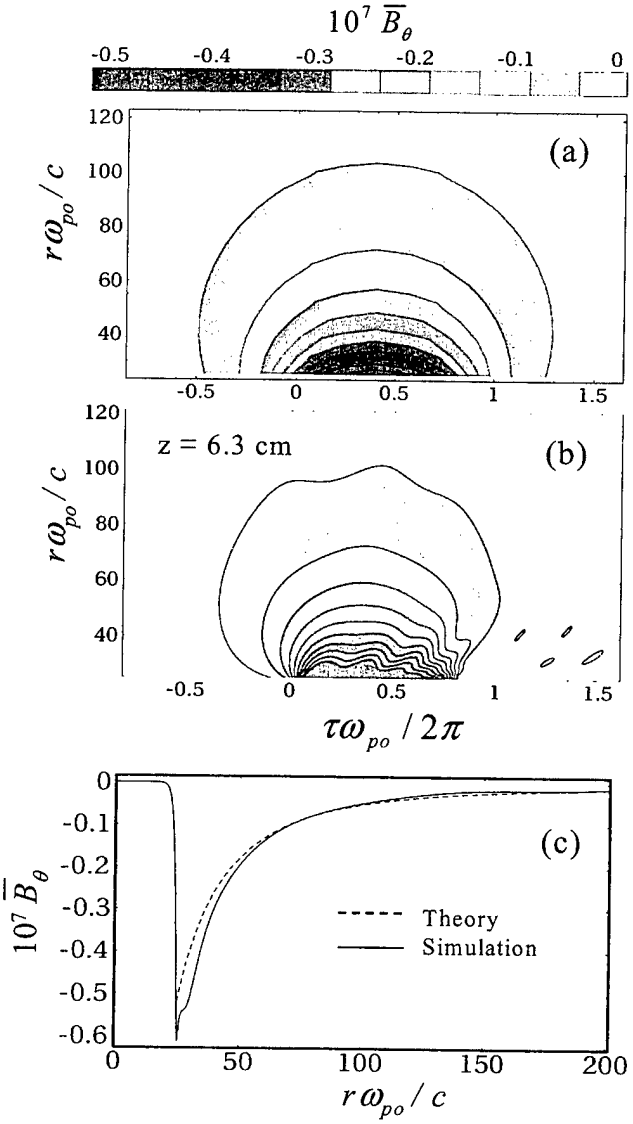


Figure 9: Comparison of normalized EMP magnetic field $\overline{B}_\theta = |q| B_\theta / mc\omega_0$ obtained from numerical simulation and steady state analysis. Panels (a) and (b) show $\overline{B}_\theta$ in the (τ, r) plane obtained from steady state analysis and numerical simulation, respectively. Panel (c) shows $\overline{B}_\theta$ vs. normalized radial position at $\tau\omega_{po}/2\pi = 0.4$ obtained from steady state analysis (dashed curve) and simulation (solid curve). Parameters are identical with those of Fig. 8.

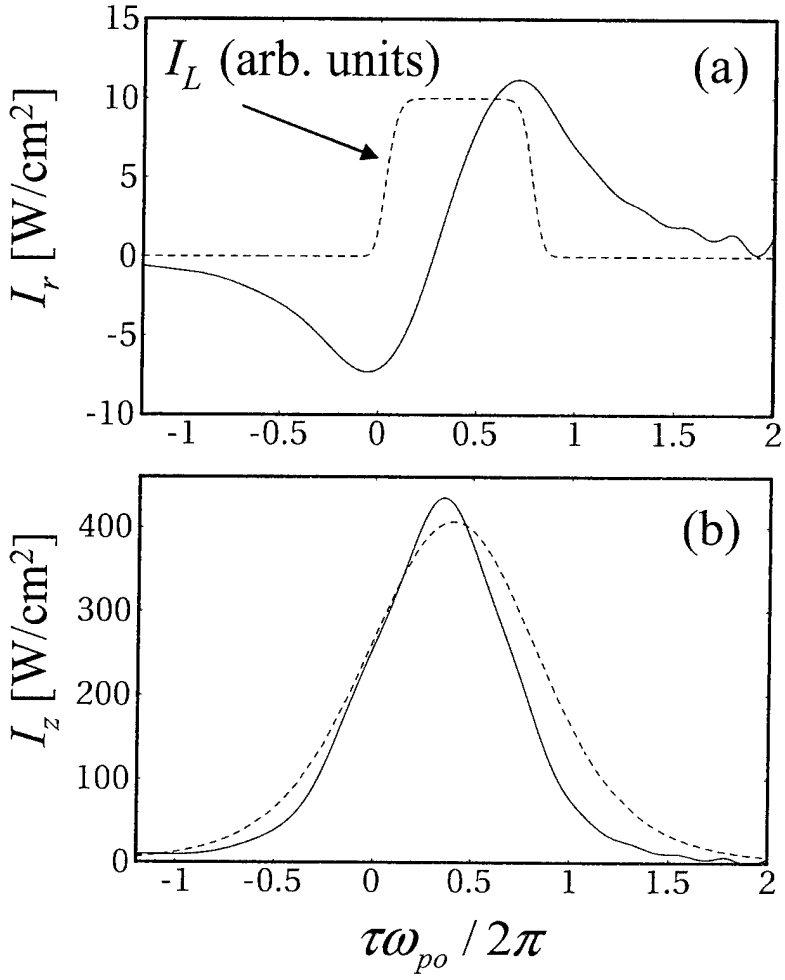


Figure 10: EMP radiance vs. normalized τ at radial position $r = 70c/\omega_{po}$ (outside the plasma filament) for the simulation of Fig. 8. Panel (a) shows radial EMP radiance, $I_r = cE_zB_\theta/4\pi$ (solid curve), and the laser intensity profile I_L (dashed curve). Panel (b) shows the axial EMP radiance, I_z (solid curve), from the simulation and the analytical calculation of $I_z = cB_\theta^2/4\pi$ (dashed curve) for steady state propagation where B_θ is obtained from Eq. (39).

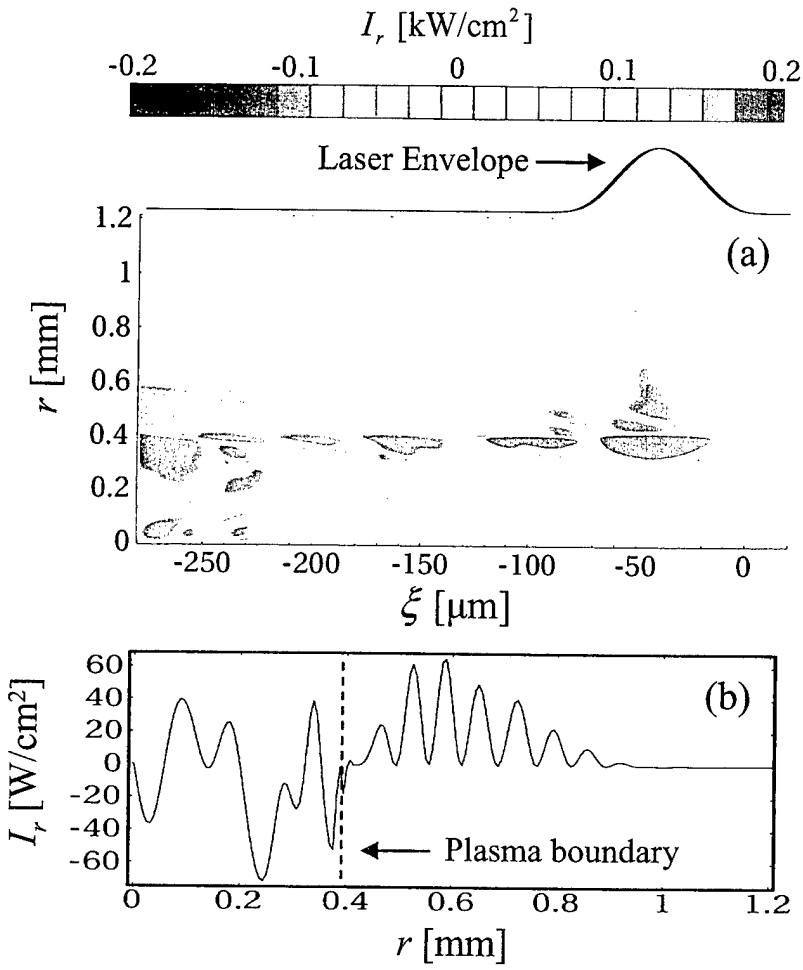


Figure 11: (a) Shaded contours of radial power flux, I_r, as a function of $\xi = z - \mathrm{v}_g t$ and radial position, r, showing radiative EMP from a modulated plasma filament with plasma density $n_{eo} = 1.1\times10^{17}$ cm^{-3} and radius $r_p = 0.4$ mm. (b) I_r vs. radial position at axial position $\xi = -220$ μm. The plasma modulation is characterized by amplitude $\varepsilon = 0.3$ and wavenumber $K = \omega_p / 4c$ as defined by Eq. (47). Laser parameters are $\lambda = 0.8$ μm, $I_{L0} = 7\times10^{13}$ W/cm^2, $\tau_L = 267$ fsec, and $\gamma_g = 109$.

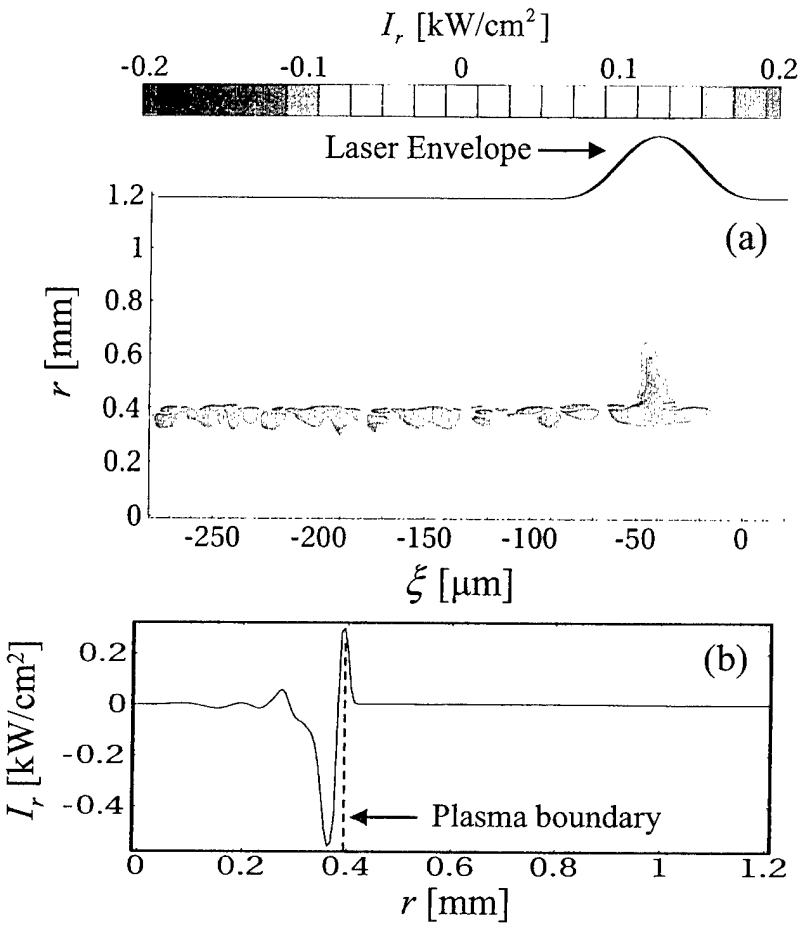


Figure 12: (a) Shaded contours of radial power flux, I_r, in the (ξ, r) plane at a propagation distance $z = 2.2$ cm in a modulated plasma filament with plasma density $n_{eo} = 1.1\times10^{17}$ cm^{-3} and radius $r_p = 0.4$ mm. The plasma modulation is characterized by amplitude $\varepsilon = 0.3$ and wavenumber $K = 4\,\omega_{po}/c$ as defined by Eq. (47). (b) I_r vs. radial position at axial position $\xi = -220$ μm. Laser parameters are $\lambda_o = 0.8$ μm, $I_{L0} = 7\times10^{13}$ W/cm^2, $\tau_L = 267$ fsec, and $\gamma_g = 109$. Note that the EMP behind the laser pulse is confined within the plasma filament. The outward radial flux observed within the laser pulse ($-80\,\mu\text{m} < \xi < 0$) is a manifestation of transient interaction at the air-vacuum interface at $z = 0$.

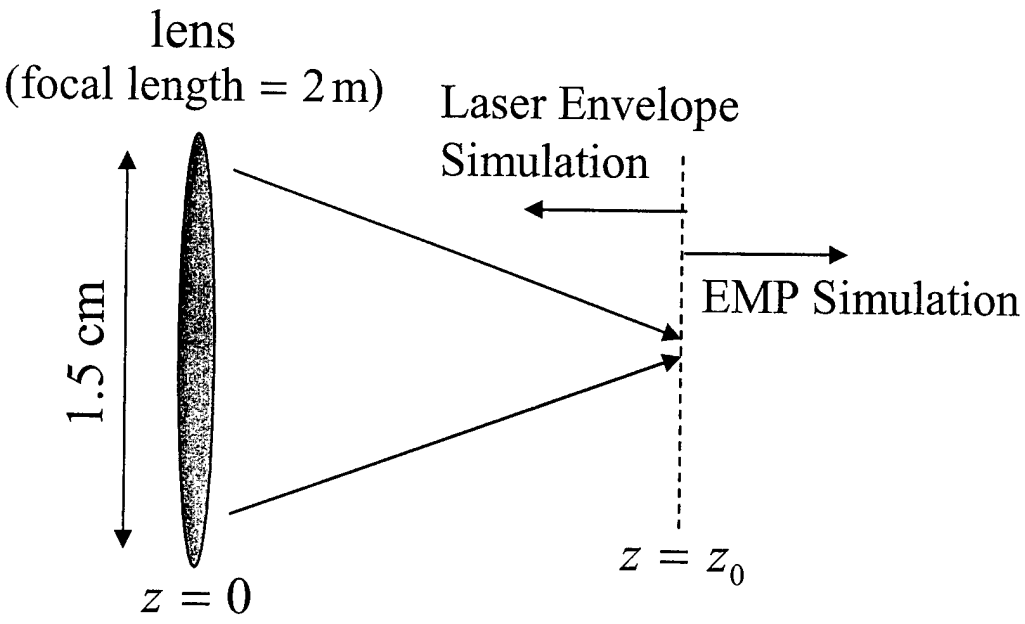


Figure 13: Schematic diagram of the simulation of the EMP experiment of Ref. 17. The laser envelope simulation (without EMP) is performed from $z = 0$ to $z = z_0$, where $z_o = 1.82$ m. The full EMP simulation is carried out for $z > z_o$.

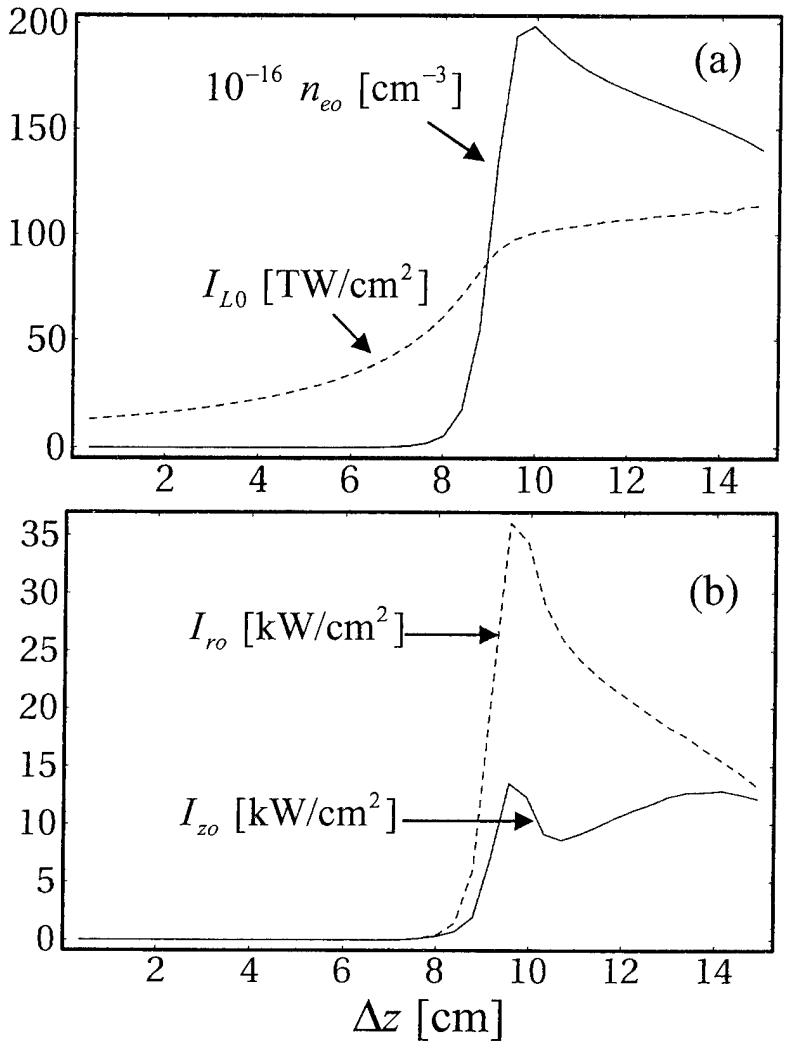


Figure 14: (a) Peak plasma density and laser intensity vs. propagation distance $\Delta z = z - z_o$ for the simulation of the experiment of Ref. 17. (b) Peak radial (dashed curve) and axial (solid curve) Poynting flux vs. Δz. Initial $(z = 0)$ laser parameters for the simulation are $\lambda_o = 0.8\ \mu\text{m}$, $P_L = 83$ GW, $\tau_L = 120$ fsec (FWHM), and $R_o = 7.5$ mm. Parameters for air are taken to be $n_o - 1 = 2.7\times10^{-4}$, $n_K = 3\times10^{-19}$ cm^2/W, $U_{ion} = 12$ eV, $\ell = 8$, and $I_{MP} \sim 10^{14}$ W/cm^2.

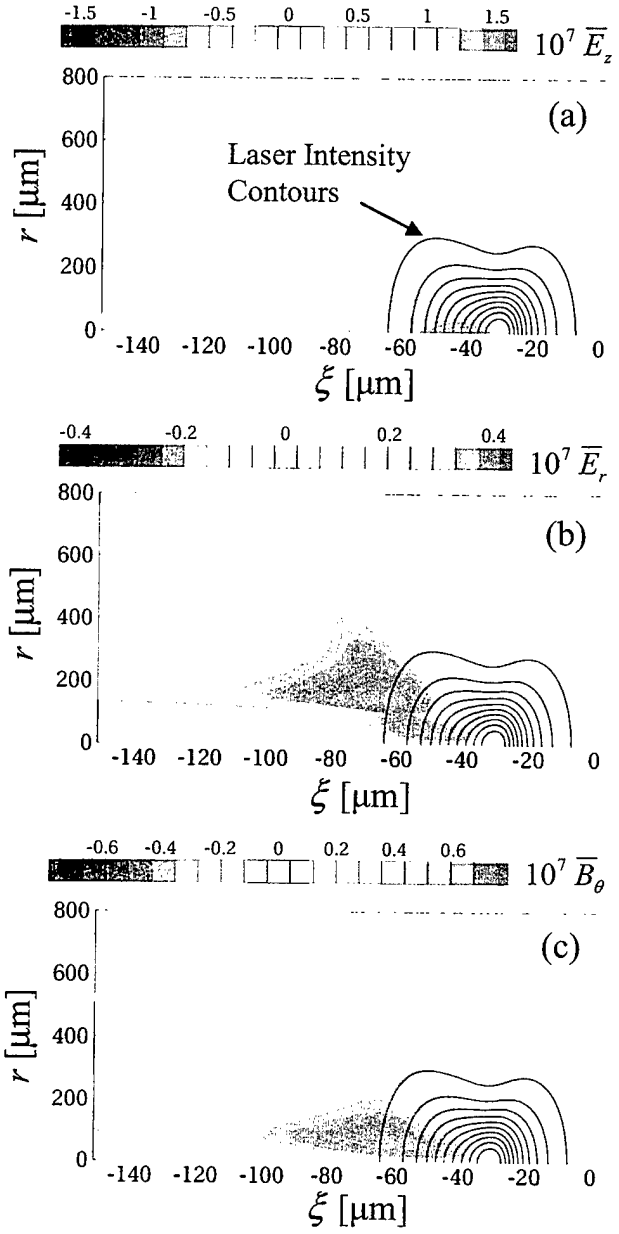


Figure 15: Contours of normalized EMP fields, (a) $\overline{E}_z = |q| E_z / mc\omega_0$, (b) $\overline{E}_r = |q| E_r / mc\omega_0$, and (c) $\overline{B}_\theta = |q| B_\theta / mc\omega_0$ as a function of $\xi = z - \mathrm{v}_g t$ and radial position, r, at propagation distance $\Delta z = 10$ cm corresponding to the simulation of Fig. 14. Unshaded contours indicate the laser intensity distribution.

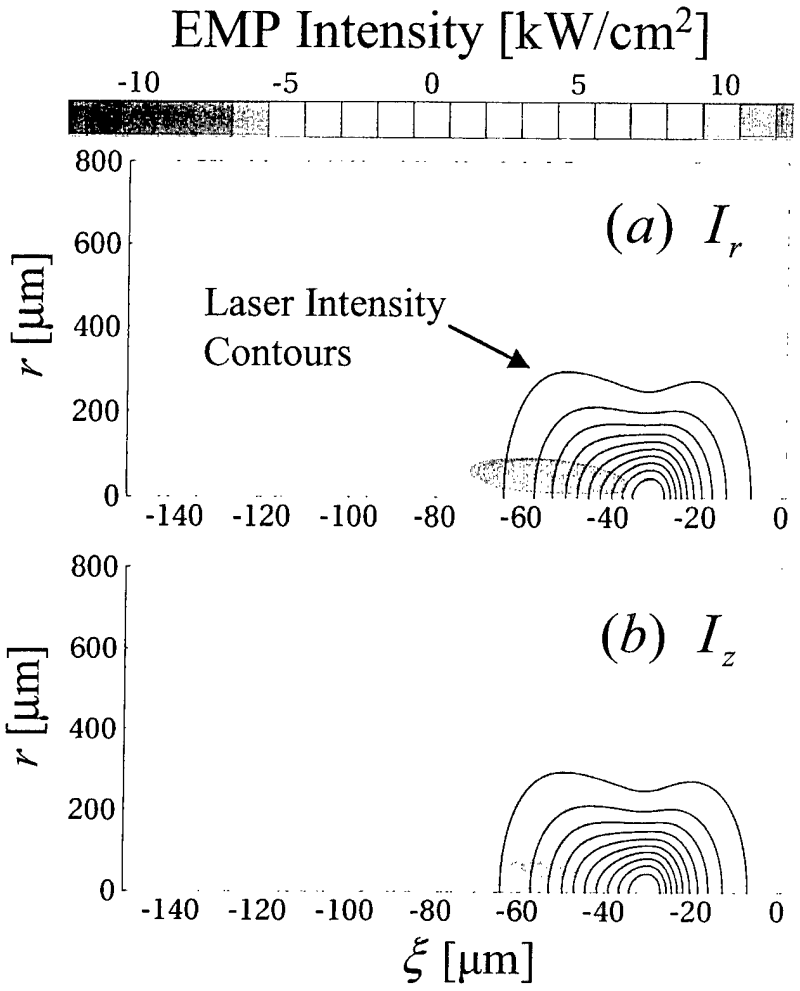


Figure 16: Contours of (a) radial and (b) axial EMP radiance as a function of $\xi = z - v_g t$ and radial position, r, at propagation distance $\Delta z = 10$ cm corresponding to the simulation of Fig. 14. Unshaded contours indicate the laser intensity distribution.

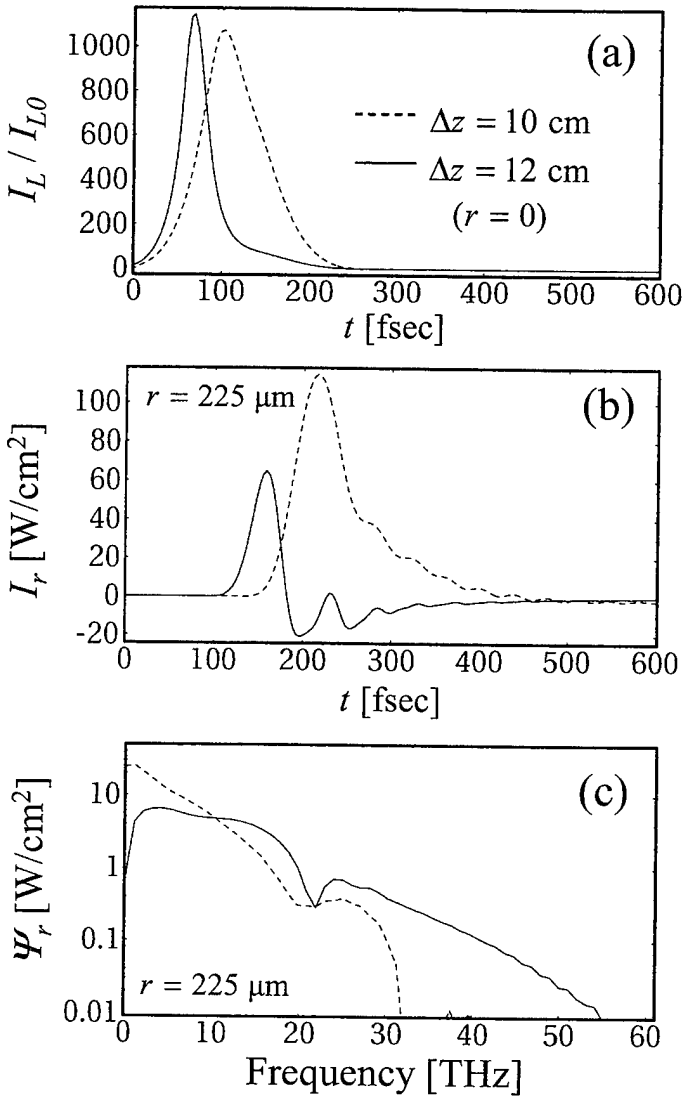


Figure 17: (a) Normalized on-axis laser intensity vs. time, (b) radial EMP Poynting flux, I_r, at radial position $r = 225\,\mu m$ vs. time, and (c) corresponding temporal Fourier transform of I_r for propagation distances $\Delta z = 10$ cm (dashed curve) and 12 cm (solid curve). The radial position $r = 225\,\mu m$ is outside of the plasma filament. Simulation parameters correspond to those listed for Fig. 14.

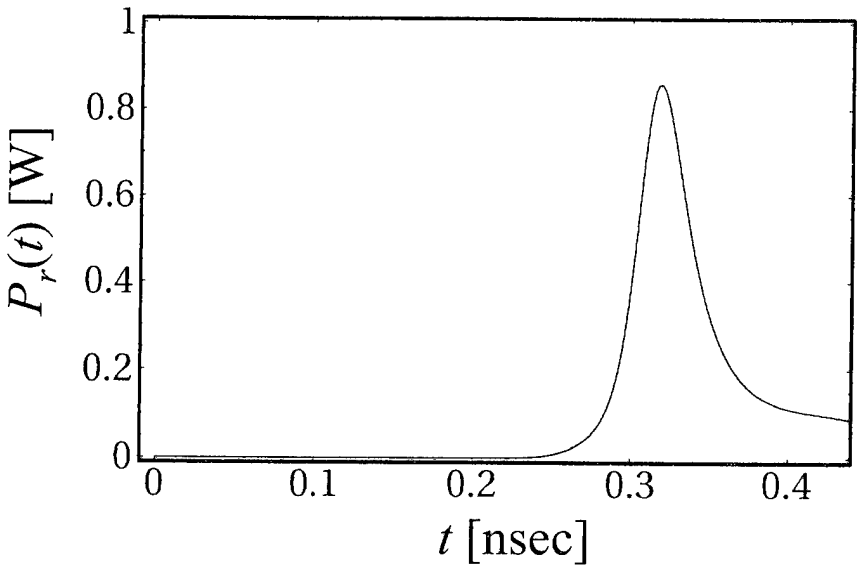


Figure 18: Total EMP power emitted radially as a function of time for the simulation of the experiment of Ref. [17]. Simulation parameters correspond to those listed for Fig. 14.

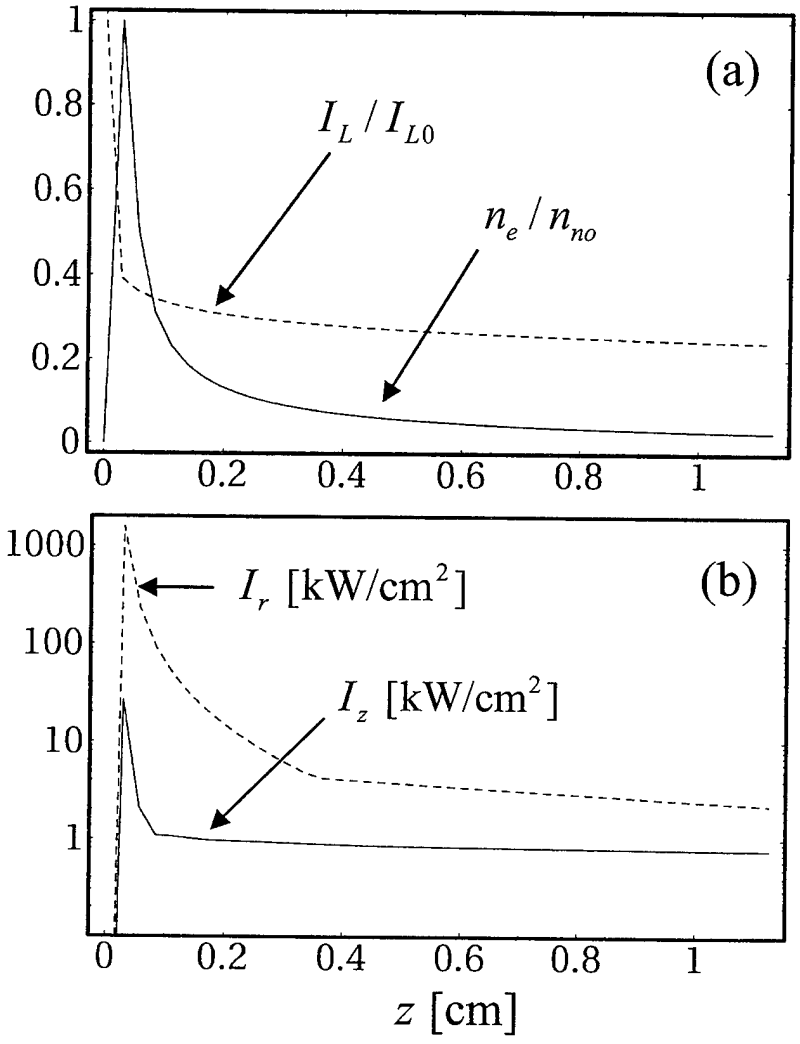


Figure 19: (a) Normalized peak laser intensity, I_L / I_{L0} (dashed curve) and normalized peak plasma density n_e / n_{no} as a function of propagation distance for an initially collimated laser pulse with $\lambda_o = 0.8$ μm, $P_L = 5.3$ TW, $\tau_L = 240$ fsec, and $R_o = 1$ mm. Parameters for air are taken to be $n_o - 1 = 2.7\times10^{-4}$, $n_K = 3\times10^{-19}$ cm^2/W, $U_{ion} = 12$ eV, $\ell = 8$, $I_{MP} = 10^{14}$ W/cm^2. (b) Corresponding peak radial (dashed curve) and axial (solid curve) Poynting flux as a function of propagation distance.

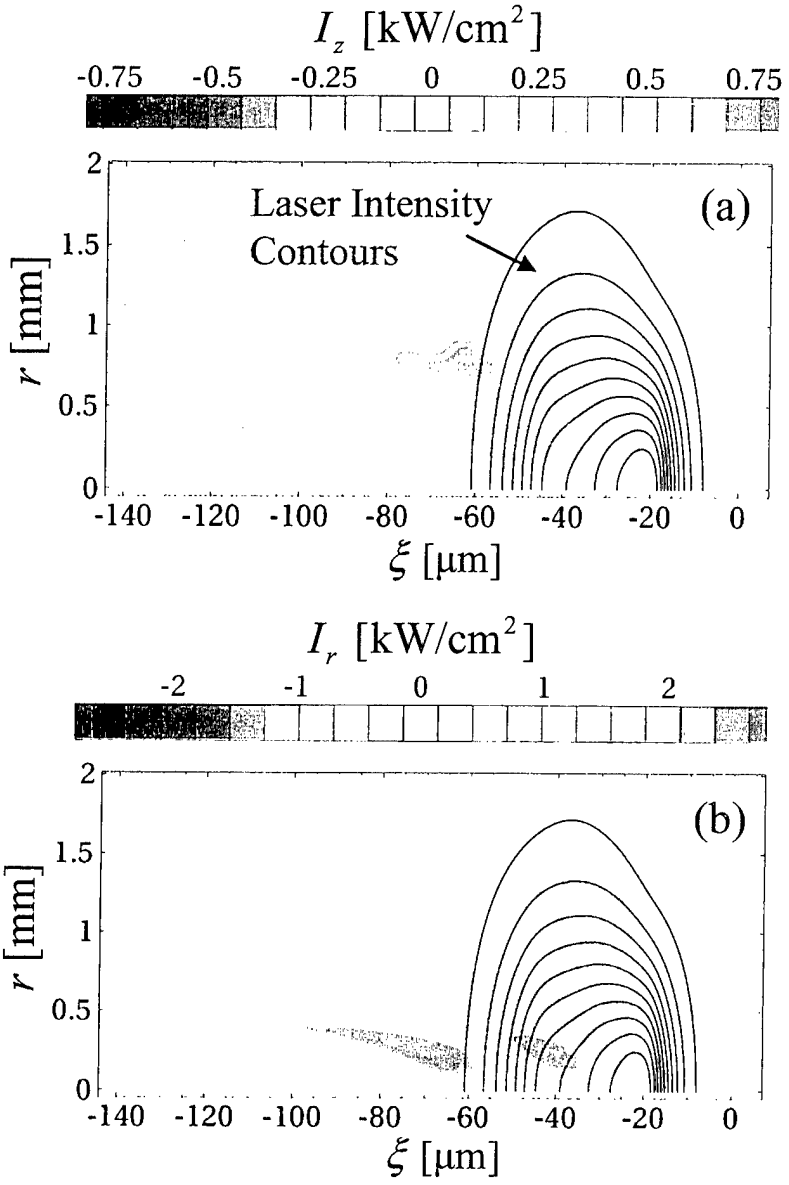


Figure 20: Contours of laser intensity (unshaded) and (a) axial and (b) radial Poynting flux (shaded contours) in the (ξ, r) plane at propagation distance $z = 0.8$ cm corresponding to the simulation of Fig. 19.

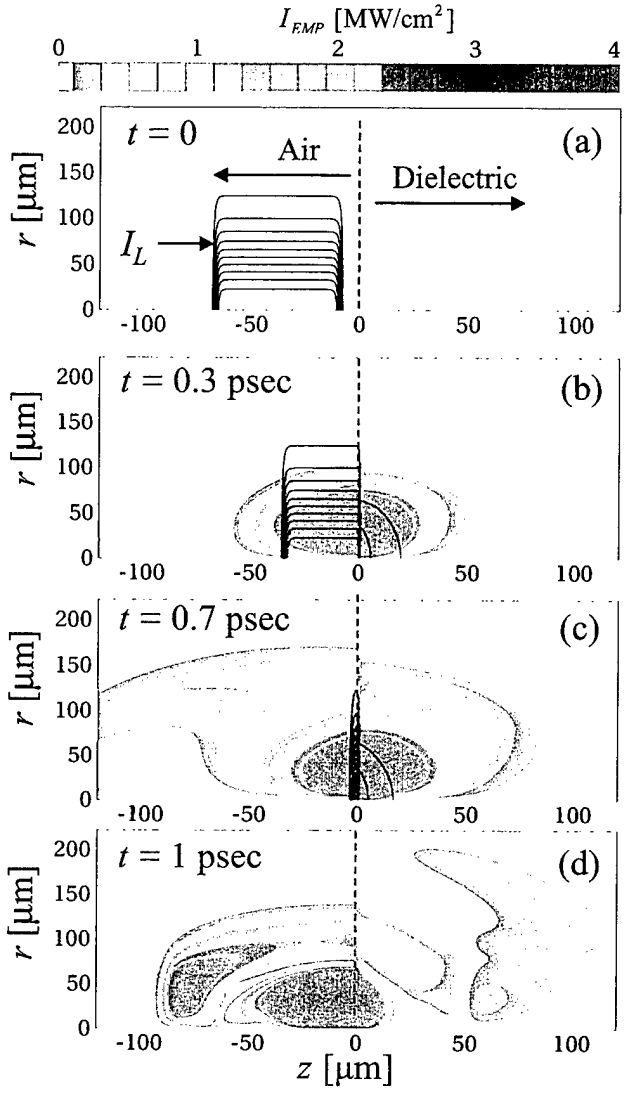


Figure 21: Simulation of EMP generation from a dielectric surface. Panels show laser intensity (unshaded contours), and total EMP flux $I_{EMP} = (I_r^2 + I_z^2)^{1/2}$ (shaded contours) in the (z,r) plane at times (a) $t = 0$, (b) $t = 0.3$ psec, (c) $t = 0.7$ psec, and (d) $t = 1$ psec. Dashed line at $z = 0$ indicates the boundary between air ($z < 0$) and dielectric ($z > 0$). Laser parameters at $t = 0$ are $\lambda_o = 0.8$ μm, $I_{L0} = 10^{13}\ W/cm^2$, $\tau_L = 200$ fsec, and $R_o = 0.1$ mm. Parameters for the dielectric are taken to be $n_o = 3$, $n_K = 7 \times 10^{-15}$ cm^2/W, $U_{ion} = 3$ eV, $\ell = 2$, $I_{MP} = 5 \times 10^{14}$ W/cm^2.